Dynamic Characterization and Modification of the Modal Properties of MEMS Structures

by

Ilgar Veryeri

A Thesis Submitted to the
Graduate School of Engineering
In Partial Fulfillment of the Requirements for
The Degree of

Master of Science
in
Mechanical Engineering

Koç University

June 2009

Koc University

Graduate School of Sciences and Engineering

This is to certify that I have examined this copy of a master's thesis by

Ilgar Veryeri

and have found that it is complete and satisfactory in all respects,
and that any and all revisions required by the final
examining committee have been made.

Committee Members:

_____

İpek Başdoğan, Ph. D. (Advisor)

_____

Çağatay Başdoğan, Ph. D.

_____

B. Erdem Alaca, Ph. D.

Date: _____

ABSTRACT

Micro Electro Mechanical Systems (MEMS) have found many application areas in different disciplines and took their place among the most promising technologies. The performance of such systems is primarily related to their dynamical characteristics. This study presents the dynamic characterization techniques that are used to identify the modal parameters of a MEMS device and the methods that can be implemented to change its dynamic response. Two distinct microscanners were chosen as the case study to demonstrate the developed methodologies. Initially, the microscanners were characterized using experimental modal analysis techniques to obtain frequency response function, modal damping, resonance frequencies, and mode shapes. Then, velocity and position feedback control loops were introduced to the scanner system to alter the damping characteristics and the resonance frequencies of the structure.

A closed-loop Simulink model of the scanners is developed to verify the experimental measurements. Several curve fitting methods are used in order to have an accurate representation of the scanner system. Using the model, the influence of both position and velocity feedback on the effective damping, resonance frequency and the transient behavior of the scanners is investigated. The stability limits of the scanners under velocity feedback are also studied via numerical simulations.

Based on the experimental and simulation results, the methodology developed in this study proves itself to be very efficient to alter the dynamical characteristics of the MEMS structures and it can be easily adapted to other MEMS applications.

ÖZET

Mikro Elektro Mekanik Sistemler (MEMS), farklı disiplinlerde birçok uygulama alanı bulmuş ve en çok gelecek vaat eden teknolojiler arasında yerini almıştır. Bu sistemlerin performansı, büyük oranda dinamik özellikleriyle bağlantılıdır. Bu çalışma, bir MEMS aygıtının modal parametrelerini belirlemek için kullanılan dinamik karakterizasyon tekniklerini ve aygıtın dinamik tepkisini değiştirmek amacıyla uygulanabilecek metotları sunmaktadır. Geliştirilmiş yöntemleri göstermek için örnek durum çalışması olarak iki farklı mikro tarayıcı kullanılmıştır. Başlangıçta, deneysel modal analiz teknikleri kullanılarak, mikro tarayıcıların frekans tepki fonksiyonları, modal sönümlenme katsayıları, rezonans frekansları ve mod şekilleri saptanmıştır. Daha sonra, yapının sönümlenme özellikleri ve rezonans frekanslarını değiştirmek için tarayıcı sistemine hız ve pozisyon geri besleme döngüleri eklenmiştir.

Deneysel ölçümleri doğrulamak amacıyla, kapalı sistem bir Simulink modeli geliştirildi. Tarayıcı sisteminin gerçeğe yakın bir temsilini elde etmek için, çeşitli eğri oturtma metotları kullanıldı. Bu modeli kullanarak, hem hız hem de pozisyon geri beslemelerinin, tarayıcıların efektif sönümlenmesine, rezonans frekanslarına ve geçici tepkilerine etkisi tetkik edildi. Hız geri beslemesi altında sistemin kararlılık limitleri sayısal benzetimlerle de ayrıca incelenmiştir.

Deney ve benzetim sonuçlarına dayanarak, bu çalışmada geliştirilmiş olan yöntemin, MEMS yapılarının dinamik özelliklerini değiştirmede çok verimli olduğu kanıtlanmıştır ve diğer MEMS uygulamalarına da kolaylıkla aktarılabilir.

ACKNOWLEDGEMENTS

I would like to express my sincere gratitude to my thesis advisor Dr. İpek Başdoğan for giving me the opportunity to work in this project and all the support she provided throughout my graduate studies. I am grateful to Dr. Çağatay Başdoğan and Dr. B. Erdem Alaca for both their endless support and taking part in my thesis committee. I also would like to thank Dr. Hakan Ürey for providing some of the experimental equipments from his research laboratory.

I have great regard for Ozan Anaç, İhsan Günev, Murat Senan and of course Bekir Yenilmez since they shared their valuable knowledge with me. Great thanks to Bilal Örün, Erdem Yüksel, Gülşen Kamçı, Sina Öcal, Umut Özcan, Baybora Baran and Yunus Emre Has for their friendship until the end of my graduate days; as laboratory partners, it has always been a pleasure to share most of our moments. I would like to thank Tolga Bayrak and İsmail Filiz for their friendship in all the indoor and outdoor activities. I also give my special thanks to Çınar Ersanlı for his endless understanding and companionship and Kübra Çürüksulu for her pure sincerity.

I would like to thank my most intimate friends Onur Miskbay, Mecit Noyan and Hasan Deniz for their existence in my life; it was always been a breath of fresh air to know that you were somewhere out there if not necessarily near me.

Last, but definitely not least, I would like to send my deepest appreciation and love to my mom, dad and sister for giving me their greatest support and endless encouragement all over my life. I cannot imagine how all of these would have happened without you.

TABLE OF CONTENTS

LIST OF TABLES

LIST OF FIGURES

Chapter 1

INTRODUCTION

Many compact visual displays or scanning devices utilize micro scanners rotating about one or two axes. Also, for several applications utilizing optical switches, projectors, head-up and head-worn displays, barcode readers, endoscopic cameras, the dynamical characteristics of micro scanners play a crucial role in the output performance of these systems [1]-[4]. The dynamical response of a micro scanner is related to its energy storage (i.e. stiffness) and dissipation capacity (i.e. damping), which in turn may affect the scanning range and resolution, the transient response and signal to noise ratio.

A micro scanner is specifically designed and manufactured based on the requirements of an application. In most of the scanners designed today, electromagnetic, electrostatic, thermal or piezoelectric actuators are used. Electromagnetic actuators work based on the forces created by a current passing through a coil in an electromagnetic field. While moving-coil actuators [5] are more popular, there are also moving-magnet actuators [6], where the coils are stationary. In electrostatic scanners, on the basis of capacitive actuation, the excitation force can be produced either by using parallel plate [7] or comb-drive actuators [8]. Comb-drive actuation is the most common technique used in micro scanners because of its relatively compact structure. On the other side, thermal actuators typically ground on the difference in thermal expansion coefficients of two materials attached to

each other [9]. The structural deformation under temperature changes is used to generate motion. While there are different thermal actuator designs and numerous applications they are used, the major weakness is the slow response times. Finally, in piezoelectric actuators, piezo crystals are used, which most basically convert any mechanical stress to electric potential and vice versa [10]. They require higher voltages for smaller deflections with respect to other types of actuators; hence they are usually preferred for high precision motions. All of these actuator approaches have their own benefits and drawbacks. However, achieving an optimum design that satisfies both the space constraints and the dynamical requirements of the application is not trivial and still the subject of research. Even if this is achieved, the same scanner cannot be easily used in another application having different dynamical requirements.

Throughout this study, an electromagnetic and an electrostatic scanner are used. The electromagnetic scanner is a moving-coil scanner, placed between a magnet and a ferromagnetic material. It is fabricated on an FR4 substrate, commonly used for printed circuit boards [11]. The electrostatic scanner is a comb-drive actuated scanner, manufactured by Mirrorcle Technologies Inc. The dynamical characteristics such as the operation frequency, quality factor and the settling time are among the design parameters of micro scanners that should be highly taken into consideration. For that purpose, a closed loop velocity and position feedback system is introduced in order to change the effective damping and stiffness characteristics of the scanners.

While methods for controlling the effective damping and stiffness of macro systems have been developed during the last decade, it has been recently applied to micro/nano systems such as micro-gyroscopes, micro-resonators and scanning AFM probes [12, 13]. The necessity to alter the system parameters in micro systems may arise from several reasons, one of which is the fabrication imperfections [14]. One of the novel methods to handle variations in resonance frequency due to fabrication imperfections in a micro-

resonator is to use an inbuilt sensor and tuner, which are thin films deposited on the hinges of the resonator [15]. The piezoelectric sensor placed at the hinges of the resonator detects small shifts in resonance frequency. The variations in the frequency are compensated by the tuner, which changes the effective spring constants of the hinges through inverse piezoelectric effect. Since the compensation through the tuner is limited, only small changes are possible. Another study demonstrated that velocity feedback can dramatically improve the dynamic response and external disturbance rejection of an electromagnetic micro-resonator [16]. The motional current output of the micromechanical resonator is electronically sensed by a sense electrode, converted to a voltage, and then added to or subtracted from the driving input signal to change the effective damping of the resonator. Improving the transient response is another reason for using velocity feedback. For example, in electrophotographic processes, widely used in laser printers where an array of surface micromachined cantilever beams are generally required, velocity feedback is also employed. This approach improves the settling time of the micro beams and reduces the image banding, a type of image artifact due to variations in the velocities of scanners [17]. Another example of velocity feedback usage is in electrostatically actuated parallel plate capacitors where low damping may result in long settling times or undesired electrode contact [18]. Most of the earlier studies discussed above have successfully implemented either position or velocity feedback to change the resonance frequency or the damping characteristics of a micro resonator.

In order to alter the dynamics effectively, the modal characteristics of the scanner must be well-understood. For that purpose, before implementing the velocity and position feedbacks, the micro scanners are dynamically characterized using experimental modal analysis techniques and the natural frequencies, quality factors and the mode shapes of the systems are identified [19]. Dynamic characterization technique of micro systems and part of the experimental system was developed in an earlier study [20]. This study has focused

on changing both the frequency and damping by investigating the influence of velocity and position feedbacks on the dynamic response of the scanners through experiments and numerical simulations.

In experimentation, the true velocity of the scanner is directly measured using a Laser Doppler Vibrometer (LDV) [21]. The velocity signal is then amplified by an adjustable gain through an analog circuit and fed back to the system to change the effective damping of the scanner. This approach is more robust especially if the nonlinear effects due to friction or external forces significantly influence the output response of the scanner. Under these circumstances, phase shifting and simply scaling the position signal to obtain the velocity signal is not a reliable approach.

Among the studies surveyed in the literature, very few investigated the dynamic response of a micro scanner under position and velocity feedback through numerical simulations supported by experiments [22]. To better understand the influence of velocity and position feedback gains on the vibratory response of the scanner, numerical simulations are performed in Simulink®. A transfer function of the scanner is developed based on the experimental frequency sweep data of the first two resonant frequencies. Then, the effect of changing the feedback gains on the dynamic response of the scanner is investigated. The numerical simulations enabled us to explore the system behavior under ideal conditions (free of environmental disturbances) and also determine the range of gain values that are used in the actual experiments.

The summary of the chapters included in the thesis is as follows:

In chapter 2, the fundamental theory covering the actuation of the scanners and the feedback are explained. The performance characteristics of a vibratory system and their alterations under the influence of feedback gains are mentioned.

Chapter 3 includes the interpretation of the experimental instruments and the software utilized throughout the study. The feedback circuit and the functioning of its parts are described in detail. Moreover, the signal flow through the circuit and the connections are explained.

The experimental procedure and the subsequent steps are summarized in chapter 4. The limitations related to the excitation voltages, data acquisition and characterization processes are explicated and the current mode shapes are identified. The frequency response curves and the experimental feedback results of the scanners are also shown in this chapter.

Chapter 5 summarizes the model development and the simulation process for the feedback. The steps of fitting a transfer function to the system are described for several techniques and a Simulink® model is built. Finally, the simulation results are compared with the experimental ones, the similarities and the dissimilarities between the frequency response curves are particularly discussed.

Chapter 2

THEORY

In this section, the actuation principle of the microscanners and their operational characteristics are explained in detail. The feedback logic and the important factors related to the performance of a vibratory system are also presented.

2.1 Actuation Principles of the Scanners

2.1.1 Electromagnetic Actuation

The presence of a magnetic field and current induce forces both on the magnetic material that is creating the field and the conductors carrying the current. According to this principle, two types of electromagnetic scanners can be manufactured; moving-coil scanners and moving-magnet scanners. The actuation of a moving coil scanner, which is used in our experiments, is performed by the creation of Lorentz forces.

In a magnetic field '*B*', the magnetic force '*dF*' acting on a particle with a charge '*dq*' and instantaneous velocity '*v*' is dq(v×B) (see Equation 2.1). Integrating Equation 2.3, the total force acting on a wire with a length '*L*' and a current '*I* ' passing through it is found to be L(I×B) (see Figure 2.1 and Equation 2.4). The Lorentz force is always perpendicular to the plane formed by the current and the magnetic field, while its direction is dependent on the direction of the current. In a proper configuration, this force can be used to vibrate a scanner under oscillating currents.

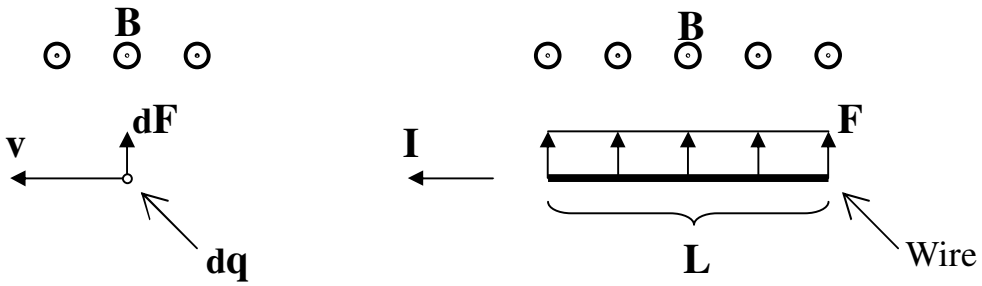

Figure 2.1 – Schematic of the Lorentz force acting on a particle and a wire.

$$dF = dq\,(\,v \times B\,) = (dq.v) \times B \tag{2.1}$$

$$I = dq\,/\,dt \quad \& \quad v = dL\,/\,dt \;\rightarrow\; dq.v = dL.I \tag{2.2}$$

$$dF = (dq.v) \times B = (dL.I) \times B = dL\,(I \times B) \tag{2.3}$$

$$F = L\,(\,I \times B\,) \tag{2.4}$$

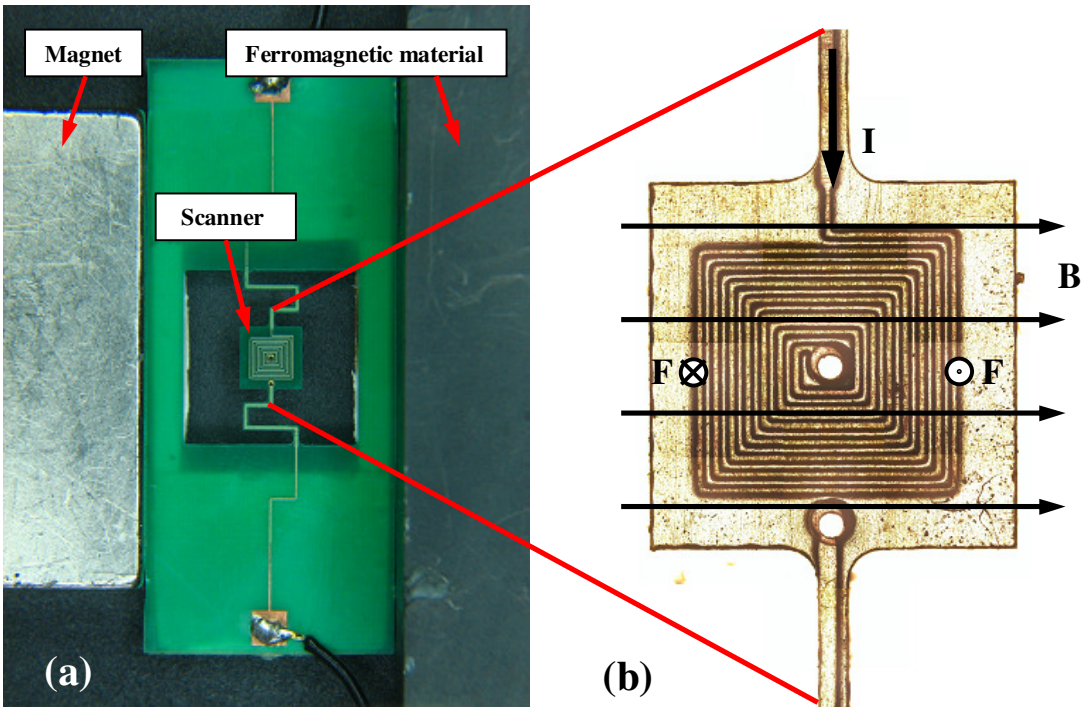

Figure 2.2: (a) Magnetic scanner's photo (b) Schematic of the magnetic scanner.

The motion of the scanner will differ due to the forces acting on its coil, in accordance with how the magnetic materials are placed. In the current setup, there is one magnet and one ferromagnetic material placed on the opposite sides of the scanner to satisfy the uniformity of the field through the coil (see Figure 2.2). To maximize the torsional motion amplitudes and to eliminate the rocking motion, the magnetic field lines are kept perpendicular to the flexures and parallel to the scanner's surface. However, due to fabrication irregularities and slightly misplaced components, the effect of several mode shapes other than the torsional one can be observed on the frequency response function (FRF). Since the electromagnetic field and the length of the coil are constant throughout the experiment, the sole variable to control the forces on the scanner is the current. By applying a sinusoidal current, it is possible to vibrate the scanner under the effect of sinusoidal forces.

2.1.2 Electrostatic Actuation

There are two types of electrostatic scanners, being actuated by the parallel plate or the comb-drive actuators. Both of these actuators work based on the capacitive effects. In this study, a comb-drive actuated scanner is used (Mirrorcle Technologies Inc, model S0107) (see Figure 2.4). The actuation is achieved by combs on both fixed and the mobile parts of the actuator (see Figure 2.3). A voltage difference (V) creates electrostatic forces (F_{es}) causing the combs to attract each other. Number of the combs (N), facing area of adjacent combs and the applied voltage are the factors which affect the force. The only controllable variable is the voltage value and it has no linear proportionality with the electrostatic force according to Equation 2.5, where dC/dx is the change in capacitance with respect to the displacement. Nevertheless, the combs are mostly designed such that the electrostatic forces are linearized with respect to the applied voltages up to a displacement value.

$$F_{es} = N\frac{1}{2}\frac{dC}{dx}V^2 \tag{2.5}$$

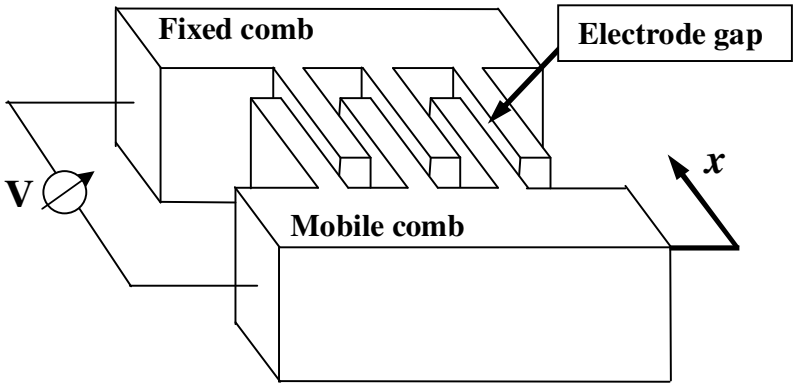

Figure 2.3: Schematic of the combs

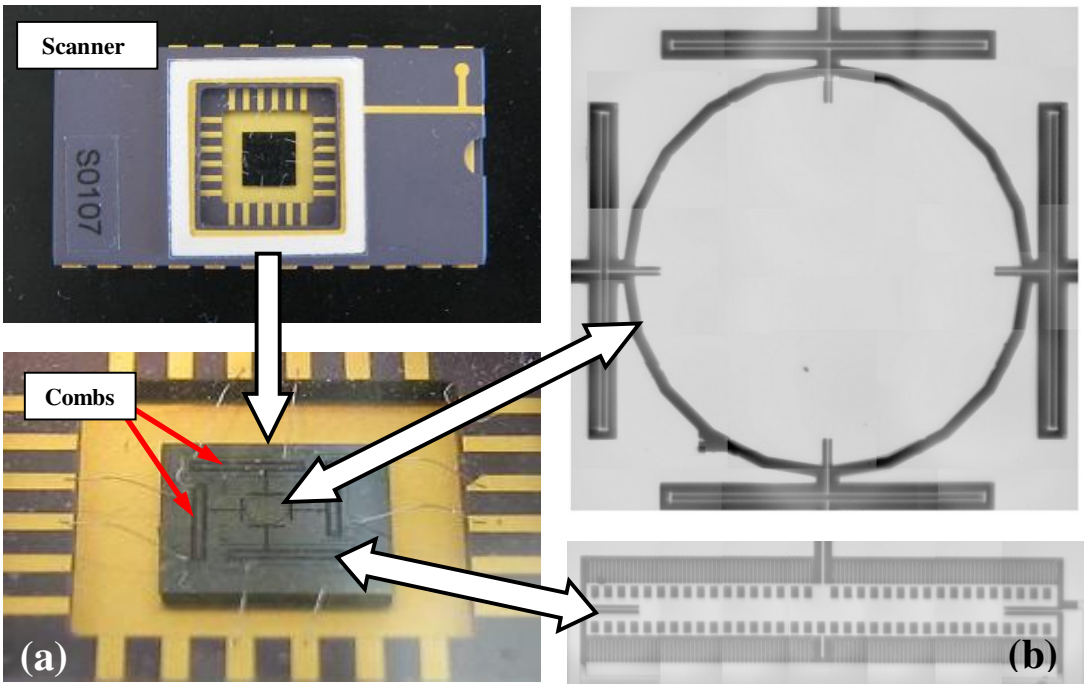

Figure 2.4: (a) Electrostatic scanner's photo (b) CCD camera images of the electrostatic scanner and the combs

2.2 Measurement of the Rotational Displacement

$$I_o.sin(wt) \rightarrow T_o.sin(wt) \rightarrow \theta_o.sin(wt + \phi) \tag{2.6}$$

The current 'I' applied to the electromagnetic scanner (or the voltage 'V' applied to the electrostatic scanner) creates a torque 'T' with the same frequency, forcing the scanner to rotate by an amount of 'θ' with a phase difference 'ϕ' (see Equation 2.6). Although the torque amplitude 'T_o' can not be observed, measuring only the rotational angle and its phase difference is satisfactory for finding out the system characteristics. The equation of motion for both systems is:

$$I\ddot{\theta}(t) + b_T\dot{\theta}(t) + k_T\theta(t) = T(\theta) \tag{2.7}$$

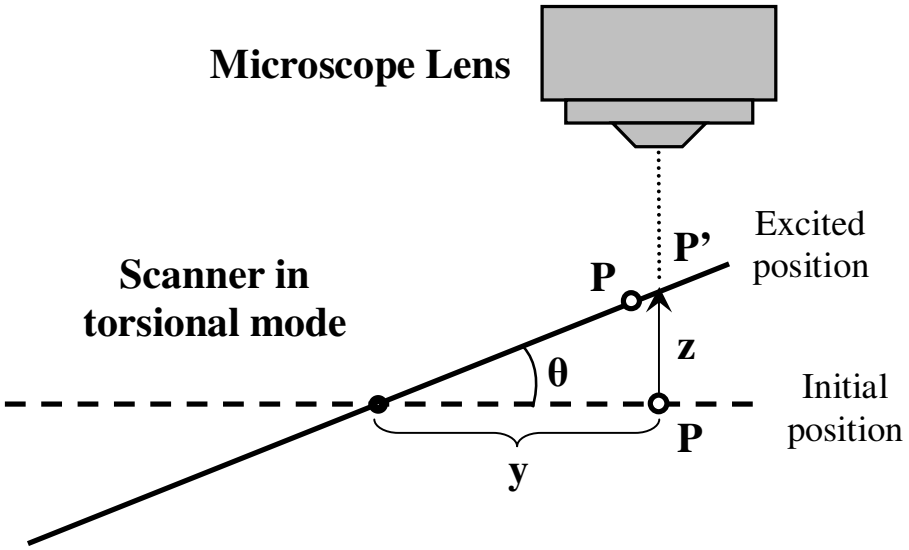

Figure 2.5: Schematic of the scanner under torsional mode. (y is constant)

$$tan(\theta) = z / y \tag{2.8}$$

$$tan(\theta) \approx \theta \text{ for small } \theta \rightarrow z \approx y.\theta \tag{2.9}$$

In the experiments, the translational motion of a point is measured, rather than the rotational motion mentioned in the Equation 2.7. The rotational displacement can be calculated from the measured translational motion (see Equation 2.8); however in feedback loops, this kind of calculation is omitted for small angles (see Equation 2.9). The system is assumed to be a point mass making pure translation in the z direction (point P' rather than the point P) (see Figure 2.5). This simplification causes an error at a level of 5% for almost 30 degrees of rotational displacement. For the case that our scanners are driven within the rotational limit of 10 degrees in our experiments, the level of error as a result of this assumption is 0.5% (see Figure 2.6).

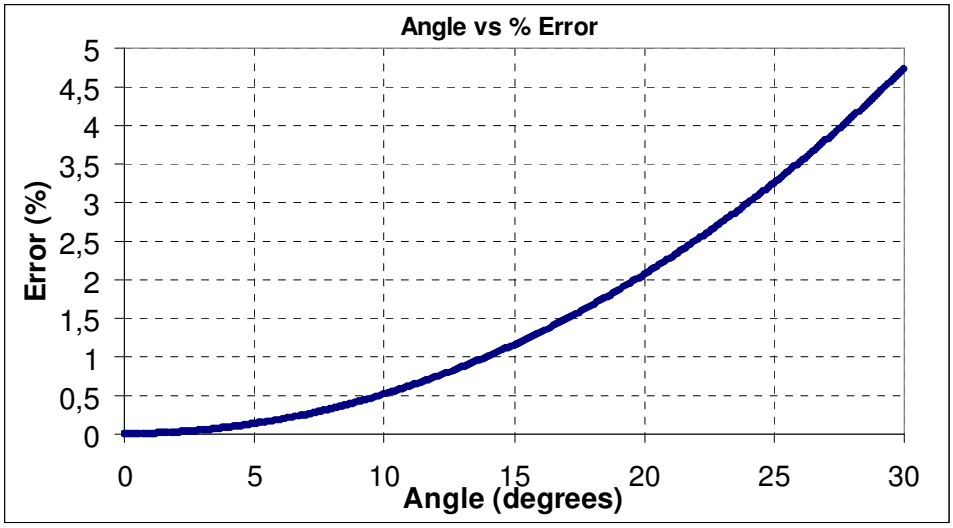

Figure 2.6: Percent measurement error with increasing angle.

2.3 Dynamical Characteristics

After the scanner is modeled as a spring-mass-damper system, the equation of motion for the measurement point without a feedback loop can be expressed as in Equation 2.10,

$$M_{eff}.\ddot{z}(t)+b.\dot{z}(t)+k.z(t)=F(z) \tag{2.10}$$

where M_{eff}, b and k are the effective mass, damping coefficient and spring constant for a specific vibration mode, respectively. The solution for Equation 2.10 is expressed in Equation 2.11. If any of the position ($z(t)$), velocity ($\dot{z}(t)$) or acceleration ($\ddot{z}(t)$) information is known, the other ones can simply be calculated by differentiation or integration. (see Equations 2.11-2.13).

$$z(t) = Z_0.sin(\omega t + \phi) \tag{2.11}$$

$$\dot{z}(t) = \omega.Z_0.cos(\omega t + \phi) = \omega.Z_0.sin(\omega t + \phi + \pi/2) \tag{2.12}$$

$$\ddot{z}(t) = -\omega^2.Z_0.sin(\omega t + \phi) = \omega^2.Z_0.sin(\omega t + \phi + \pi) \tag{2.13}$$

Concerning the performance of an oscillatory mechanical system; the natural frequency (ω_n), the quality factor (Q) and the time constant (τ) values should be taken into consideration (see Equations 2.14-2.16). The quality factor determines the rate of energy dissipation relative to the working frequency and it is inversely proportional to the damping ratio of the system. The time constant is a measure that indicates how fast the system settles within 2% of a certain value.

$$\omega_n = \sqrt{\frac{k}{M_{eff}}} \tag{2.14}$$

$$Q = \frac{1}{2.\xi} = \frac{M_{eff.}\omega_n}{b} \tag{2.15}$$

$$\tau = \frac{1}{\xi.\omega_n} = \frac{2.M_{eff}}{b} \tag{2.16}$$

2.4 Velocity Feedback

The main idea behind the velocity feedback is to modify the effective damping (b'=b-G) of the system by adding the measured velocity signal multiplied by a velocity feedback gain G, to the actuation signal as given in Equation 2.17. It is seen that the pure velocity feedback modifies the quality factor and the time constant of the system, while the natural frequency remains the same (see Equations 2.18-2.20). A system with high quality

factor dumps its energy slower, resulting in higher-amplitude steady-state oscillations and a sharp resonance curve. On the other hand, low quality factors are desired for improved transient response with faster settling times [18].The method can be used either to increase the quality factor or enhance the transient response.

$$\begin{aligned} M_{eff}.\ddot{z}(t)+b.\dot{z}(t)+k.z(t)&=F(z)+G.\dot{z}(t)\\ M_{eff}.\ddot{z}(t)+(b-G).\dot{z}(t)+k.z(t)&=F(z)\end{aligned} \tag{2.17}$$

$$\omega_{n_{VF}}=\sqrt{\frac{k}{M_{eff}}}=\omega_n \tag{2.18}$$

$$Q_{VF}=\frac{M_{eff.}\omega_n}{(b-G)} \tag{2.19}$$

$$\tau_{VF}=\frac{2.M_{eff}}{(b-G)} \tag{2.20}$$

2.5 Position Feedback

Similarly, the position feedback aims the modification of the effective stiffness (k'=k-H) of the system by adding a position signal multiplied by a position gain H (see Equation 2.21). Pure position feedback affects the quality factor as well as the natural frequency; however it has no effect on the time constant (see Equations 2.22-2.24). The method can be effectively used for altering the resonant frequencies.

$$\begin{aligned} M_{eff}.\ddot{z}(t)+b.\dot{z}(t)+k.z(t)&=F(z)+H.z(t)\\ M_{eff}.\ddot{z}(t)+b.\dot{z}(t)+(k-H).z(t)&=F(z)\end{aligned} \tag{2.21}$$

$$\omega_{n_{PF}}=\sqrt{\frac{k-H}{M_{eff}}} \tag{2.22}$$

$$Q_{PF}=\frac{M_{eff.}\omega_{n_{PF}}}{b} \tag{2.23}$$

$$\tau_{PF}=\frac{2.M_{eff}}{b} \tag{2.24}$$

Chapter 3

EXPERIMENTAL SETUP

This section summarizes the instruments and the software utilized in the experiments (see Figure 3.1) and their main functions. In the feedback circuit part, the circuit elements and their details are also explained.

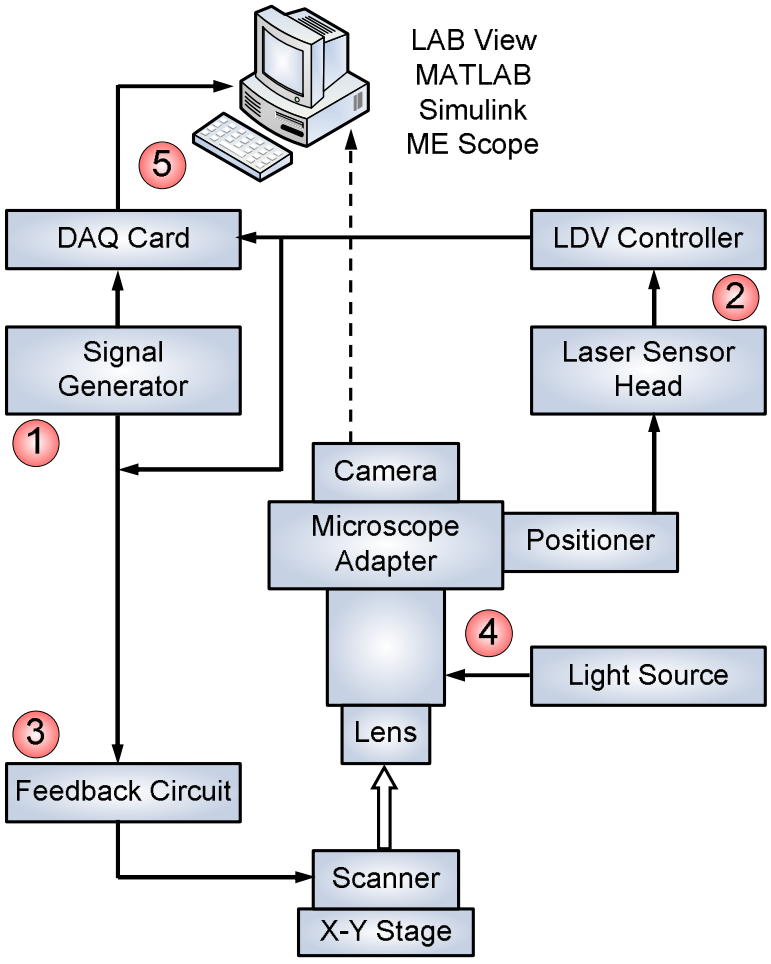

Figure 3.1: Schematic of the experimental setup.

3.1 Function Generator

Agilent 33220A is a 20MHz synthesized function generator (signal generator) with built-in arbitrary waveform and pulse capabilities. The sine function required to excite the system is generated within the frequency range 1μHz – 20MHz with 1μHz resolution. The voltage output has an upper limit of 10Vpp into a 50Ω circuit, capable to reach maximum output current value of 200mA. The function generator's output signal is transferred to the feedback circuit before being sent to the scanner.

3.2 Laser Doppler Vibrometer

The scanner's vibrational velocity and displacement in out-of-plane direction is measured by Polytec Fiber Optic Vibrometer [23], operating based on the Doppler principle, detecting back-scattered laser light from a vibrating structure. The Laser Doppler Vibrometer (LDV) consists of the OFV-551 fiber interferometer and the OFV-5000 vibrometer controller.

The OFV-551 sensor head delivers the laser light to the measurement point and collects the reflected light as an input to the interferometer by utilizing flexible fiber optic cable together with a focusing lens. It creates red laser beams with 663 nm wavelength from a He-Ne laser source and it has a spot size of 2.1μm through the use of the microscope.

The controller provides signals and power for the sensor head, and processes the vibration signals. The vibration signals are electronically converted by decoders within the controller to obtain velocity and displacement information. Since the position decoder component is not installed to the controller, only the velocity data will be gathered by the wide bandwidth velocity decoder, VD-02. The decoder has four ranges (5mm/s/V, 25mm/s/V, 125mm/s/V, 1000mm/s/V) with resolution 0.15μm/s and it can detect signals up to 10m/s with an upper frequency limit of 1.5MHz. The velocity signal is sent to the feedback circuit to be added to the function generator's output signal as a feedback component.

3.3 Feedback Circuit

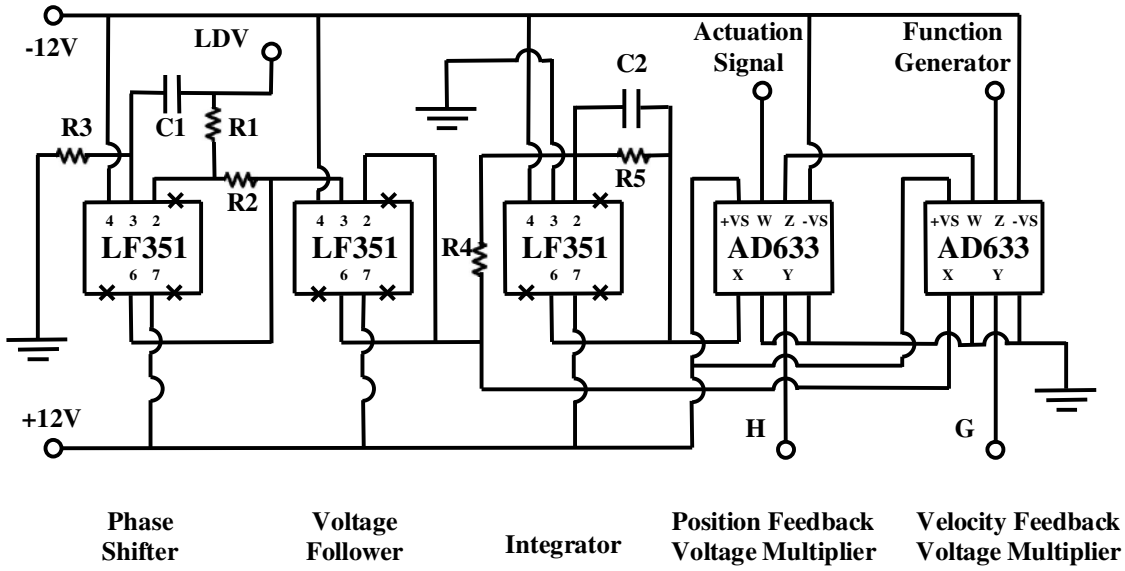

Figure 3.2: The velocity and position feedback circuit.

The mirror is actuated using a velocity and position feedback circuit as shown in Figure 3.2. The components of the feedback circuit are the phase shifter, the voltage follower, the integrator and the gain amplifiers. Their purposes and the criteria regarding the circuit's design are specified below.

3.3.1 Phase Shifter

The analog phase shifter is integrated into the signal processing circuit to adjust the phase deviations at different frequencies due to the intrinsic time delay in the LDV. The real velocity phase of the scanner and the feedback circuit's input velocity phase must either be the same or shifted 180° since otherwise will lead to an uncontrolled feedback. Although the delay observed in LDV is constant and small at the operating frequency, it increases proportionally with increasing frequency, resulting in an undesired position signal

in the velocity feedback loop and vice versa. Therefore, obtaining a true velocity signal with 0° or 180° phase shift is necessary to feedback the system properly.

In the phase shifter, STMicroelectronics wide bandwidth operational amplifier LF-351 is used (see Figure 3.3). The resistances 'R1' and 'R2', connected to the operational amplifier determine the input to output amplitude ratio. If the amplitude ratio is to be kept constant, 'R1' and 'R2' values should be taken the same and high enough to reduce the error owing to the production tolerances.

The amount of shift can be tuned by adjusting the capacitance 'C1' or the resistance 'R3' in the phase shifter circuit (see Figure 3.3). To observe the behavior of this circuit for varying resistance and capacitance values, *pSpice* circuit design program is used [24]. As shown in figure 3.4 drawn according to the *pSpice* data at a frequency 1kHz, changing either the resistance or the capacitance by the same amount individually has the same effect on the phase shift. Similarly in Figure 3.5 drawn for a capacitance value of 10nF, the same behavior is observed for frequency and resistance couple. Hence, after selecting a value for the capacitance, the resistance can be fine tuned in its allowable range to obtain a desired shift in phase at a specific frequency.

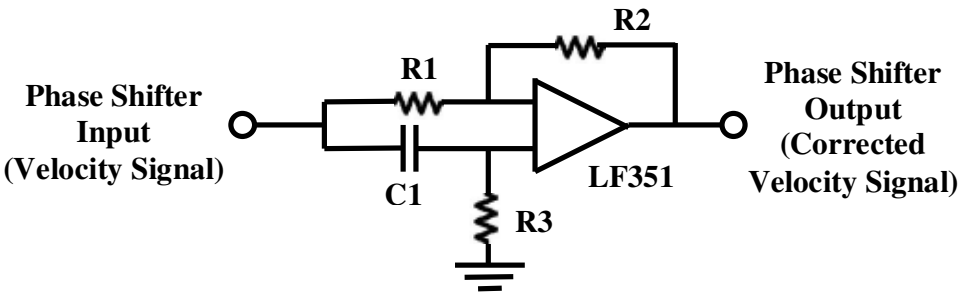

Figure 3.3: The phase shifter part of the circuit.

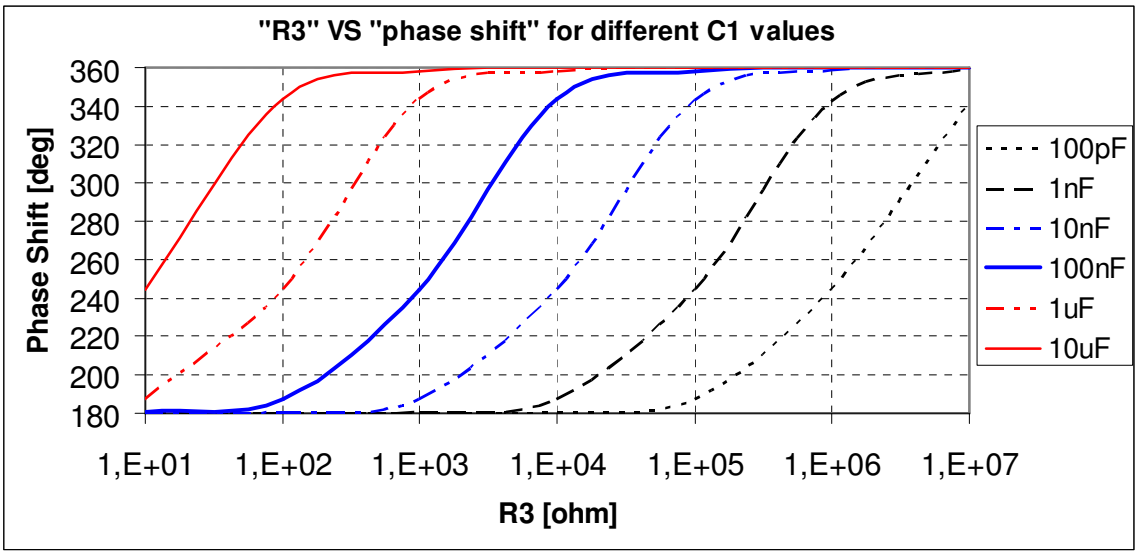

Figure 3.4: Phase shift in degrees for various values of resistance and capacitance.

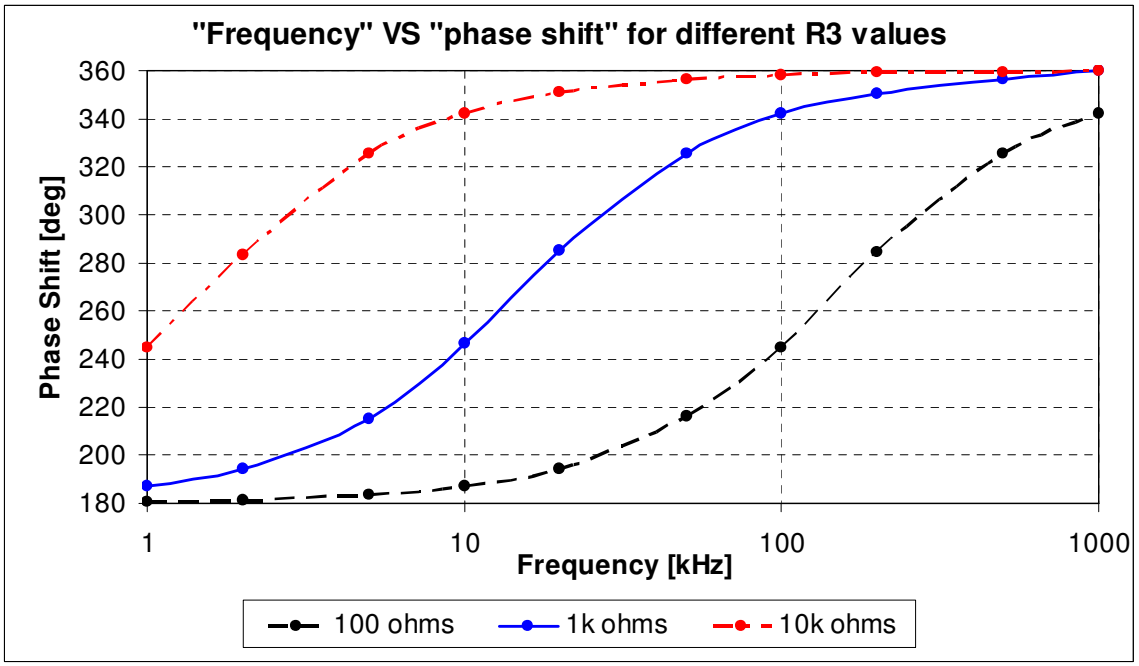

Figure 3.5: Phase shift in degrees for various values of frequency and resistance.

3.3.2 Voltage Follower

Ideally, the phase shifter's velocity output should be connected to the integrator's input to be transformed into the scaled position signal. However, in some conditions including our circuit, due to high impedance, the current at some points becomes too small. To overcome this problem, a voltage follower is placed at the output of the phase shifter (Figure 3.2). A voltage follower is again an operational amplifier (LF351) which outputs a low impedance voltage that is identical to its input. Since it reduces the impedance, the signal becomes stronger. The enhanced velocity signal is sent both to the integrator and the velocity feedback gain amplifier.

3.3.3 Integrator

For a real integration process, the phase of a sinusoidal signal should shift 90 degrees while the amplitude should be reduced by an amount of the working frequency (see Section 2.3 for details). Therefore, for a system having a resonant frequency in the orders of kHz, the integrated signal will be practically too small to observe. However, if that signal will be used for feedback purposes, a scaling factor in the integration process will be needed in order to maintain the integrator output to input ratio (O/I ratio) close to unity.

In the integrator component (see Figure 3.6), the operational amplifier LF351 is used again to modify the phase shifter's output signal. An artificial position signal is generated by integrating and scaling the measured velocity signal. There are two important points one must notice. The first one is that the phase difference between the velocity and the position signals must be very close to, if not exactly equal to 90^o (or 270^o). The second one is that the output voltage should neither be too low, since the signal could die out because of the noise; nor be too high, since the circuit's power supply or some components could not tolerate higher voltages.

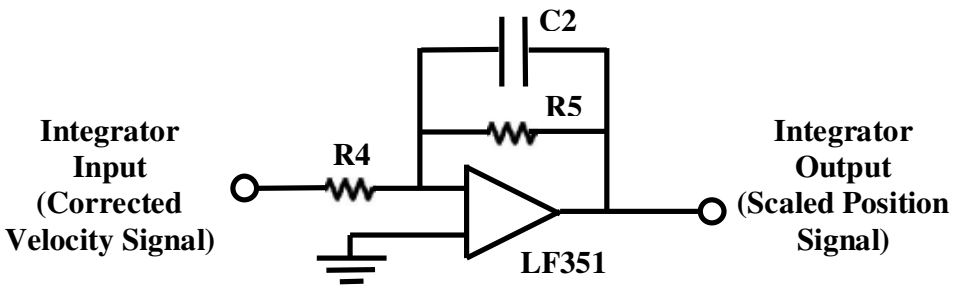

Figure 3.6: The integrator part of the circuit.

To select the right resistance and capacitance values for the integrator component of the circuit, again a *pSpice* model is developed for the phase shifter. One capacitor 'C2' and two resistors 'R4' and 'R5' affect both the amplitude and the phase simultaneously. The output signal is also dependent on the working frequency. Since there are too many independent variables to determine the output behavior of the integrator, the frequency is taken as a constant value for simplification. Initially, an array of output variables for several different C2, R4 & R5 values is formed to see the general behavior of the integrator (see Table 3.1). Briefly, increasing C2 value increases the phase difference and generally decreases the amplitude as well as decreasing the settling time; increasing R4 value decreases the amplitude while increasing R5 value increases both the amplitude and the phase difference. It must be noted that, among many possibilities, choosing a smaller capacitance value would be better for a faster transient response. After selecting the most appropriate values from the array and then trying for different frequency values, the effect of changing frequency is also seen (see Table 3.2).

Table 3.1: Integrator output variables for different R4, R5 and & C2 values.
(at 1kHz and 100mV input voltage)

	C2 :	10^-9			C2 :	10^-8			C2 :	10^-7		
R4 : 10^1	R5	Phase	Amp	Ratio	R5	Phase	Amp	Ratio	R5	Phase	Amp	Ratio
	10^1	180	100	1	10^1	180	100	1	10^1	180.3	100	1
	10^2	180	1000	10	10^2	180.3	1000	10	10^2	183.6	1000	10
	10^3	180.3	10000	100	10^3	183.6	10000	100	10^3	213	8400	84
	10^4	183.6	100000	1000	10^4	213	84000	840	10^4	261	14200	142
	10^5	213	840000	8400	10^5	261	142000	1420	10^5	271.5	14800	148
	10^6	261	1420000	14200	10^6	272	148000	1480	10^6	273	15500	155
R4 : 10^2	R5	Phase	Amp	Ratio	R5	Phase	Amp	Ratio	R5	Phase	Amp	Ratio
	10^1	180	10	0.1	10^1	180	10	0.1	10^1	180.3	10	0.1
	10^2	180	100	1	10^2	180.3	100	1	10^2	183.6	100	1
	10^3	180.3	1000	10	10^3	183.6	1000	10	10^3	213	840	8.4
	10^4	183.6	10000	100	10^4	213	8400	84	10^4	261	1420	14.2
	10^5	213	84000	840	10^5	261	14200	142	10^5	271.5	1480	14.8
	10^6	261	142000	1420	10^6	272	14800	148	10^6	273	1550	15.5
R4 : 10^3	R5	Phase	Amp	Ratio	R5	Phase	Amp	Ratio	R5	Phase	Amp	Ratio
	10^1	180	1	0.01	10^1	180	1	0.01	10^1	180.3	1	0.01
	10^2	180	10	0.1	10^2	180.3	10	0.1	10^2	183.6	10	0.1
	10^3	180.3	100	1	10^3	183.6	100	1	10^3	213	84	0.84
	10^4	183.6	1000	10	10^4	213	840	8.4	10^4	261	142	1.42
	10^5	213	8100	81	10^5	261	1420	14.2	10^5	271	148	1.48
	10^6	261	14200	142	10^6	272	1480	14.8	10^6	273	155	1.55
R4 : 10^4	R5	Phase	Amp	Ratio	R5	Phase	Amp	Ratio	R5	Phase	Amp	Ratio
	10^1	180	0.1	0.001	10^1	180	0.1	0.001	10^1	180.3	0.1	0.001
	10^2	180	1	0.01	10^2	180.3	1	0.01	10^2	183.6	1	0.01
	10^3	180.3	10	0.1	10^3	183.6	10	0.1	10^3	213	8.4	0.084
	10^4	183.6	100	1	10^4	213	84	0.84	10^4	261	14.2	0.142
	10^5	213	800	8	10^5	261	142	1.42	10^5	271	14.8	0.148
	10^6	261	1420	14.2	10^6	272	148	1.48	10^6	273	15.5	0.155
R4 : 10^5	R5	Phase	Amp	Ratio	R5	Phase	Amp	Ratio	R5	Phase	Amp	Ratio
	10^1	180	0.01	0.0001	10^1	180	0.01	0.0001	10^1	180.3	0.01	0.0001
	10^2	180	0.1	0.001	10^2	180.3	0.1	0.001	10^2	183.6	0.1	0.001
	10^3	180.3	1	0.01	10^3	183.6	1	0.01	10^3	213	0.84	0.0084
	10^4	183.6	10	0.1	10^4	213	8.4	0.084	10^4	261	1.42	0.0142
	10^5	213	80	0.8	10^5	261	14.2	0.142	10^5	271	1.5	0.015
	10^6	261	142	1.42	10^6	272	14.8	0.148	10^6	273	1.5	0.015
R4 : 10^6	R5	Phase	Amp	Ratio	R5	Phase	Amp	Ratio	R5	Phase	Amp	Ratio
	10^1	180	0.001	0.00001	10^1	180	0.001	0.00001	10^1	180.3	0.001	0.00001
	10^2	180	0.01	0.0001	10^2	180.3	0.01	0.0001	10^2	183.6	0.01	0.0001
	10^3	180.3	0.1	0.001	10^3	183.6	0.1	0.001	10^3	213	0.084	0.00084
	10^4	183.6	1	0.01	10^4	213	0.84	0.0084	10^4	261	0.142	0.00142
	10^5	213	8	0.08	10^5	261	1.42	0.0142	10^5	271	0.148	0.00148
	10^6	261	14.2	0.142	10^6	272	1.5	0.015	10^6	273	0.155	0.00155

Table 3.2: Integrator output variables for different R5 & frequency values.
(at 100mV input voltage, for R4=10kohm and C2=10nF)

	Freq : 1000 Hz			**Freq :** 1500 Hz			**Freq :** 2000 Hz		
R5	**Phase**	**Amp**	**Ratio**	**Phase**	**Amp**	**Ratio**	**Phase**	**Amp**	**Ratio**
10^1	180	0.1	0.001	180	0.1	0.001	180	0.1	0.001
10^2	180.3	1	0.01	180.6	1	0.01	180.6	1	0.01
10^3	183.6	10	0.1	187	10	0.1	187.2	10	0.1
10^4	213	84	0.84	225	70	0.7	233	60	0.6
10^5	**261**	**142**	**1.42**	**264**	**98**	**0.98**	**266**	**72**	**0.72**
10^6	**272**	**148**	**1.48**	**271**	**99**	**0.99**	**272**	**72**	**0.72**
10^7	273.5	152	1.52	274	100	1	274	74	0.74

Having analyzed the effects of the resistances and the frequency change, the approximate values for the components to be selected are determined. Although the *pSpice* simulations yielded satisfactory results, the final values are selected by fine tuning experimentally.

3.3.4 Velocity Feedback Voltage Amplifier

The voltage amplifier used in the feedback loops is Analog Devices Low Cost Analog Multiplier AD633. The transfer function of AD633 is W=X.Y/(10V)+Z where X and Y are differential inputs, Z is the summing input and W is the output of the multiplier. The scale factor of 10V is provided by a buried Zener diode in the analog multiplier.

In the velocity feedback loop, the corrected velocity signal received from the phase shifter is multiplied by a velocity gain G and added to the function generator's signal. The velocity gain is the power supply gain divided by a scale factor of 10V. The calculated output signal is sent to the position feedback voltage amplifier.

3.3.5 Position Feedback Voltage Amplifier

The generated output of the velocity feedback voltage amplifier is the summing input of the position feedback voltage amplifier. Similarly, the multiplication of the position signal received from the integrator with the position gain H is then added to this summing input. The output of the position feedback voltage amplifier is the actuation signal for the scanner. The existence of two separate feedback elements allows to feedback the system both with velocity and position data independently.

3.3.6 Circuit Board

The modifications in the circuit to reduce the noise levels are discussed below. Because of the capacitive effects occurring in the breadboards, perforated boards are used in the preliminary stages of the experiments. The circuit was placed in grounded metal plate to overcome possible electromagnetic noise. As the last configuration, the perforated board is replaced with Printed Circuit Board (PCB) and the inputs to the circuit which were formerly attached by crocodiles are substituted with female BNC connectors.

As is known, PCBs are generally copper sheets laminated onto one or both sides of a non-conductive substrate. After the required pathways are formed, the unused copper parts still remain on the board. Just for comparison purposes, the same circuit design is printed on two PCBs, engraving the unused copper of only one of the PCBs, letting the other untouched (see Figure 3.7). It is observed that the noise levels for every component in the engraved PCB are better than the other (see Table 3.3).

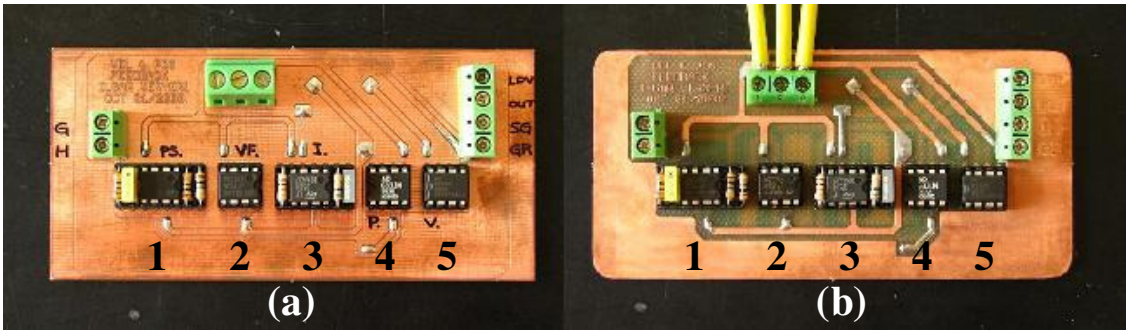

Figure 3.7: (a) The original PCB, (b) the engraved PCB.
(1.Phase shifter, 2.Voltage follower, 3.Integrator, 4.Position feedback voltage amplifier, 5.Velocity feedback voltage amplifier)

Table 3.3: Noise levels for the component outputs of two different PCBs

NOISE	original PCB	engraved PCB
Function Generator	2 - 3 mV	1 - 2 mV
Phase Shifter	8 - 10 mV	2 - 4 mV
Voltage Follower	8 - 10 mV	2 - 4 mV
Integrator	10 - 12 mV	6 - 8 mV
LDV	20 - 30 mV	8 - 10 mV

The noise level measurements for the LDV outputs are performed with the LDV decoder scale at 25mm/s/V. Since the signal amplitude values are in the range of several volts around the resonant frequency, the LDV output is obtained with an error less than 1%, an amount that will hardly affect the feedback quality.

3.4 Microscope System

Focusing and image capturing processes are performed in the microscope system. It is composed of five main parts, being VM-1V Video adaptable microscope, Meiji-S.Plan objectives, Meiji FL150 light source with halogen lamp, a CCD camera and a Polytec microscope scan unit MSV-50.

To gather visual information of a micro device, the device is placed under a microscope and a lens. VM-1V microscope can be used with all kind of infinity corrected lenses. Meiji S.Plan M5X lens is used for focusing on electromagnetic scanner and Meiji S.Plan M10X is used for electrostatic scanner. The VM-1V microscope views an area of 0.96mm x 0.72mm using 1/3" CCD camera with 5X magnification lens and an area of 0.48mm x 0.36mm with 10X magnification lens. Meiji-S.Plan M5X and M10X objectives are infinity corrected objectives with numerical apertures of 0.10 and 0.25, and depths of focus of 55μm and 8.8μm, respectively. The inline illumination of the micro devices is achieved by Meiji FL150 light source. It is a 150W halogen lamp which is used with flexible single arm light guide to be attached to the microscope.

The image of the device is captured by a CCD camera mounted on the microscope. The CCD camera is a Point Grey FLEA CCD 1/3" IEEE-1394 camera with 1024x768 pixels resolution with a pixel size of 4.65μm x 4.65μm. The location of the device is adjusted by an X-Y stage for translational velocity measurements of different points. The positioning of the laser spot can also be achieved by the Polytec microscope scan unit MSV-50 [25]. The Polytec microscope scan unit is composed of two main parts which are OFV-71 and OFV-72. OFV-72 is the microscope adapter for the camera and OFV-71 is the manual positioner for the laser beam. The microscope adapter can be equipped with a digital camera, Point Grey FLEA, to visualize the measurement object and it contains a filter to reduce the viewed intensity of the laser spot when observing mirror-like surfaces. OFV-71 is the manual positioner of the laser beam which contains movable mirrors to deflect the laser beam.

3.5 Software and Data Acquisition

The software programs used in the setup for collecting the motion information, system characterization and post-processing, primarily are LAB View 6.1, MATLAB 7.2, Simulink 6.4, and ME'Scope [26-28].

The analog signals of the function generator and the LDV controller are sent to the computer via the data acquisition card (DAQ card) capable of converting these signals to digital ones. The LAB View is used for interfacing with DAQ card which is NI 6034E to gather this digital information. In LAB View environment, it is also possible to connect to the function generator via GPIB interface. The program is used to obtain the frequency response functions of different points on the scanner by driving the function generator in a specified frequency interval.

The ME'Scope software is used to extract the modal parameters such as resonant frequencies and modal damping coefficients. By implementing the experimentally measured frequency response functions to the computer model of the micro device, flexible mode shapes can also be analyzed.

The MATLAB and the Simulink toolbox are used for system characterization and further simulations. The transfer function of the system is obtained from the frequency response functions and subsequently used by Simulink to observe the feedback characteristics without experimental limitations.

Chapter 4

IMPLEMENTATION OF VELOCITY AND POSITION FEEDBACK ON THE SCANNERS

In this section, the results of the experiments are presented. The voltage limitations of the electromagnetic and electrostatic scanners are tested prior to the feedback experiments (see Section 4.1). The dynamic characterization of the scanners is performed in Section 4.2, and then the velocity and position feedbacks are implemented to change the damping and frequency characteristics of the scanners (see Appendix A for the experimental process flow chart).

4.1 Behavior of the Scanners under Sinusoidal Voltages

4.1.1 Electromagnetic Scanner Behavior

The electromagnetic scanner can be driven by a sinusoidal input voltage only, without necessarily with a DC voltage offset. As one can recall from the theory (see Section 2.1.1), the forces acting on the scanner are linearly proportional with the amplitude of the input voltages. The velocity response of the scanner under increasing sinusoidal voltage at the resonant frequency is plotted to see the scanner's voltage limitations (see Figure 4.1). It is observed that after an input voltage of about 200 mV, the output response of the mirror becomes bounded. The experiments are carried on within the range where the response of the scanner changes linearly as a function of the input voltage.

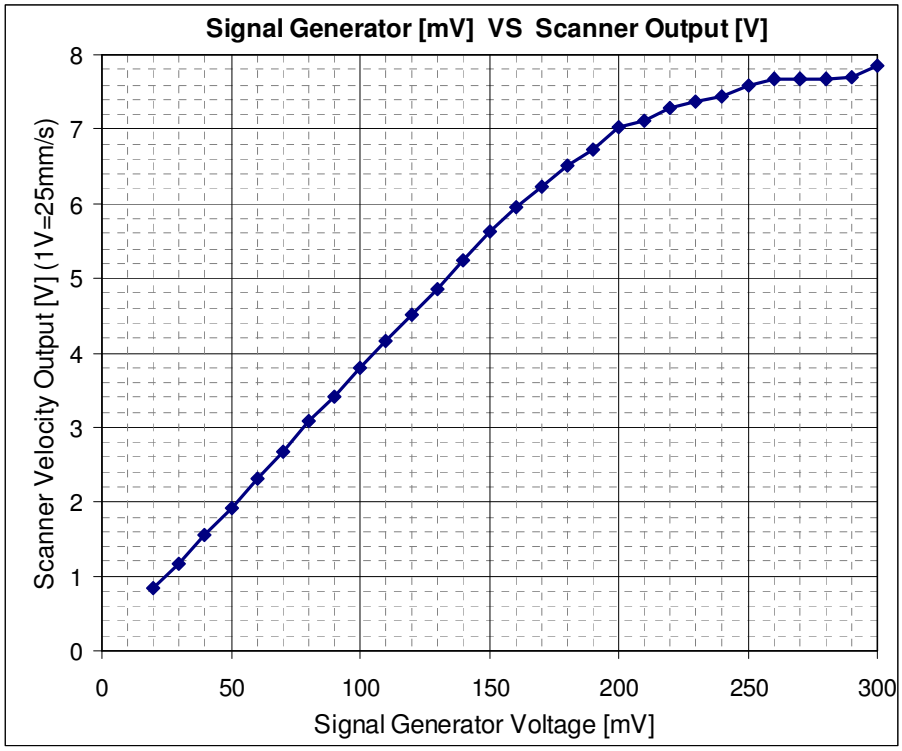

Figure 4.1: Amplitude of the electromagnetic scanner velocity for increasing input voltage.

4.1.2 Electrostatic Scanner Behavior

The electrostatic scanner requires a sinusoidal input voltage combined with a DC voltage. The reason for this is that the scanner is a one-quadrant device which is able to deflect from rest position to one side only, but not to the opposite side. Hence, only the positive excitation signals can drive the scanner. In experiments, it is critical that the sinusoidal input amplitudes always lie under the DC voltage amplitude. In the datasheet supplied from the manufacturer of the electrostatic scanner, it is stated that it can operate up to DC actuation voltages of 140V. This is not a limitation as the signal generator in our laboratory has a maximum DC voltage output of 5V. Knowing that the input voltages will not exceed total amplitude of 5V, the output response for increasing sinusoidal voltage with constant DC offset at the resonant frequency is plotted (see Figure 4.2). As it can be

observed from Figure 4.2, the scanner velocity changes linearly as a function of input voltage and does not become bounded even at the high voltages.

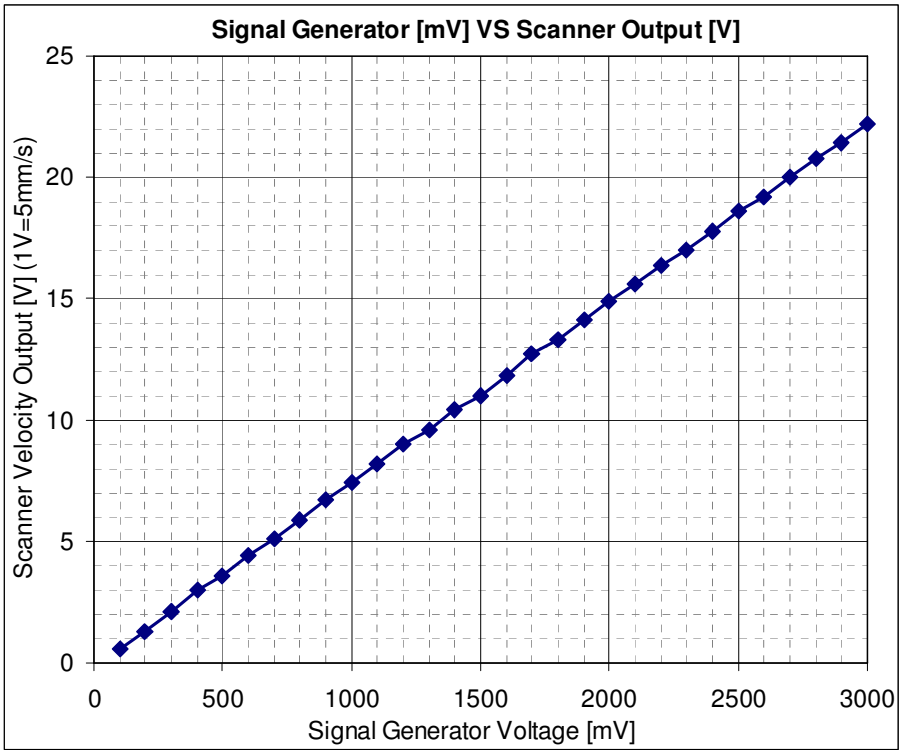

Figure 4.2: Amplitude of the electrostatic scanner velocity for increasing sinusoidal input voltage.

4.2 Dynamic Characterization of the Scanners

The exact locations of the data points are required for the repeatability of the experiments. On that account, the images captured from the surface of an individual scanner are initially joined to obtain the whole surface image. That surface image is then divided by grids and made transparent to prepare a ghost image (see Figure 4.3). The real time CCD camera image is finally matched to a suitable position on that ghost image by

MATLAB (see Appendix B for the MATLAB code). This operation enables us to direct laser beams on the desired locations of the grid surface.

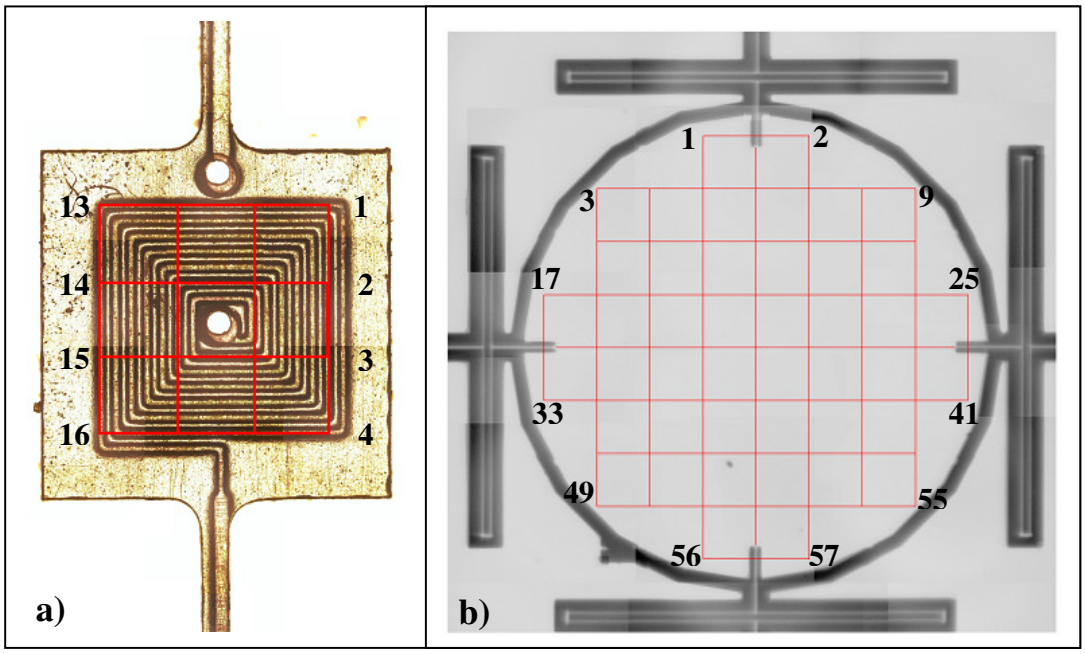

Figure 4.3 – MATLAB Ghost images with grid
(a) Electromagnetic scanner, (b) Electrostatic scanner

After the voltage limitations of the scanners are determined, the scanners are actuated by applying sinusoidal excitation voltages within a safe range. Frequency response characterization is done by sweeping the frequency of the excitation signal while keeping the amplitude constant. Throughout the sweep, the frequency, velocity amplitude of the scanning point and the phase difference between the input and output signals are recorded to obtain the frequency response curves of predefined grid locations. Driving the scanner via the signal generator, the data acquisition and recording processes are performed by a LABVIEW interface program (see Figure 4.4).

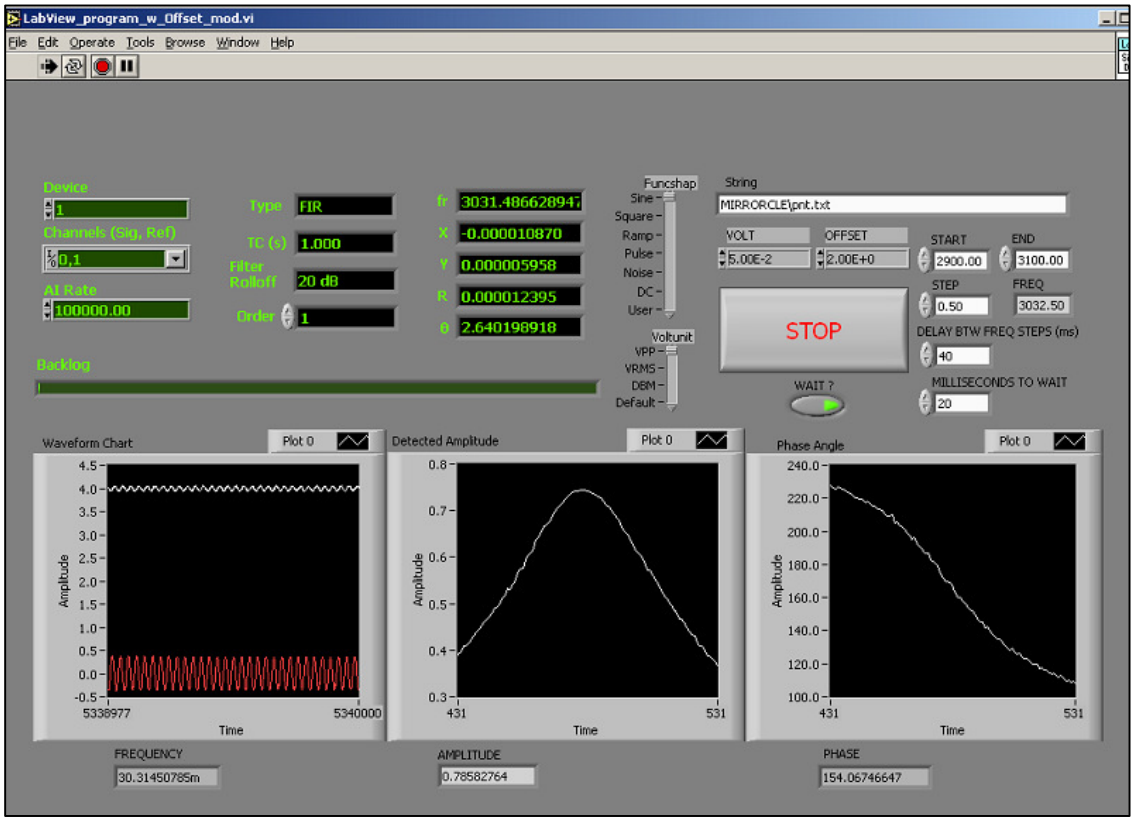

Figure 4.4 – LABview program graphical user interface (while recording sweep data)

After the amplitude and the phase difference information are recorded for all the points on the grid, they are converted into real and imaginary parts to be input to the ME'Scope program for the mode characterization (see Equation 4.1, where R is the oscillation amplitude and ϕ is the phase information). A surface model of the scanner is also built to visualize the mode shapes. The measurement data being assigned to the related points on the surface model; the program uses integrated curve fit techniques to match a model to the experimental frequency response functions (see Figure 4.5 - red curves). Finally, the modal analysis is performed to estimate the mode shape and the modal parameters for the second resonance mode.

$$R.e^{i\phi} = R.cos(\phi) + i.R.sin(\phi) \tag{4.1}$$

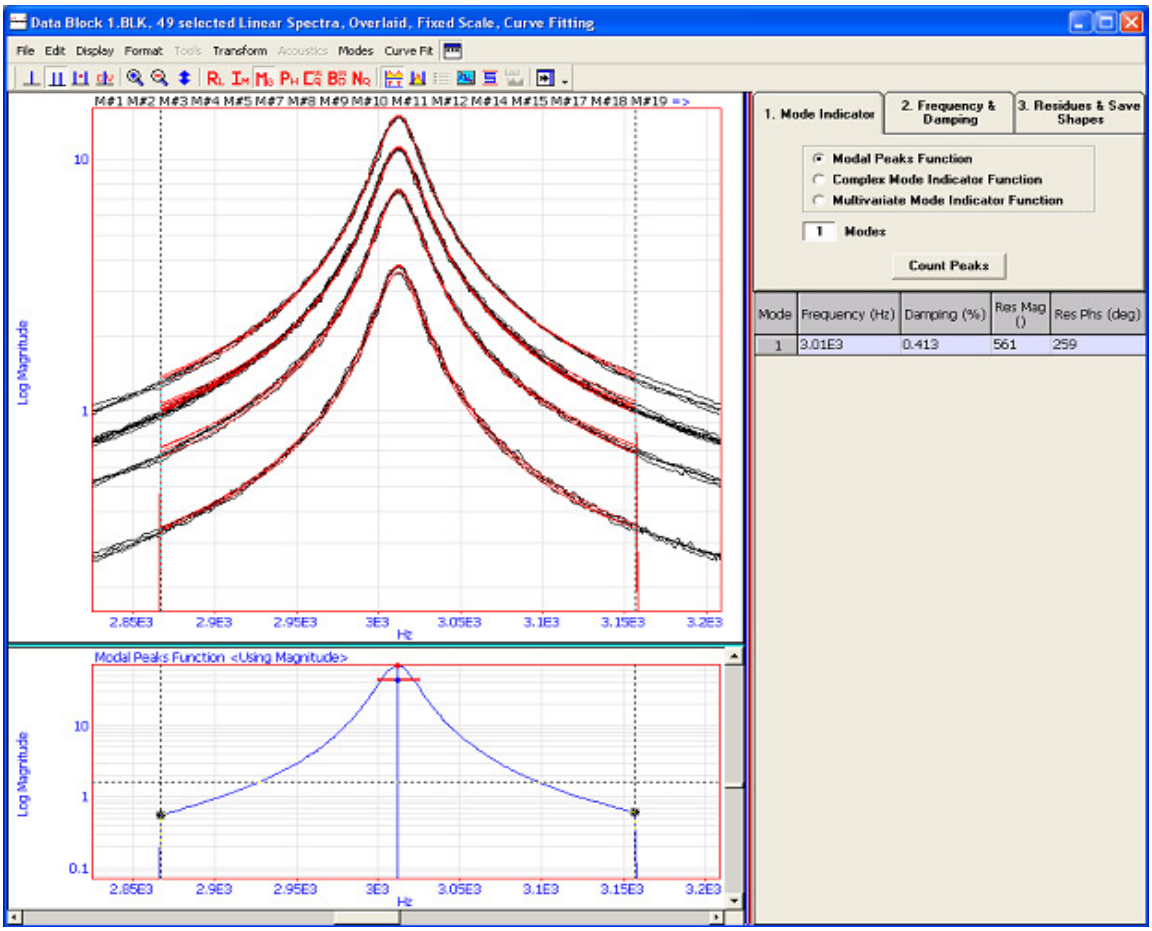

Figure 4.5: Screenshot of ME'Scope while curve fitting to the experimental FRFs.

The torsional modes of the electromagnetic and the electrostatic scanner are shown in Figure 4.6 and the modal damping ratios (ξ) are found 0.755% (Q=66.2) and 0.413% (Q=121.1) by ME'Scope, respectively. The Q values related to that mode are calculated using the damping ratios by Equation 4.2. The quality factor of a system can be also defined as the ratio of the natural frequency (ω_n) to the bandwidth at half power ($\Delta\omega$) of

that resonance [29] (For electromagnetic scanner, Q = 1442/22 = 65.5 and for electrostatic scanner, Q = 3011/25.1 = 120, from the experimental FRFs). The comparison of Q values calculated both by Equations 4.2 and 4.3 shows that they are very close to each other. Frequency response curves for point 1 on electromagnetic scanner and point 17 on electrostatic scanner are plotted in Figure 4.7 and 4.8, respectively.

$$Q = 1 / (2\xi) \quad \textit{(using ME'Scope)} \tag{4.2}$$

$$Q = \omega_n / \Delta\omega \quad \textit{(using FRFs)} \tag{4.3}$$

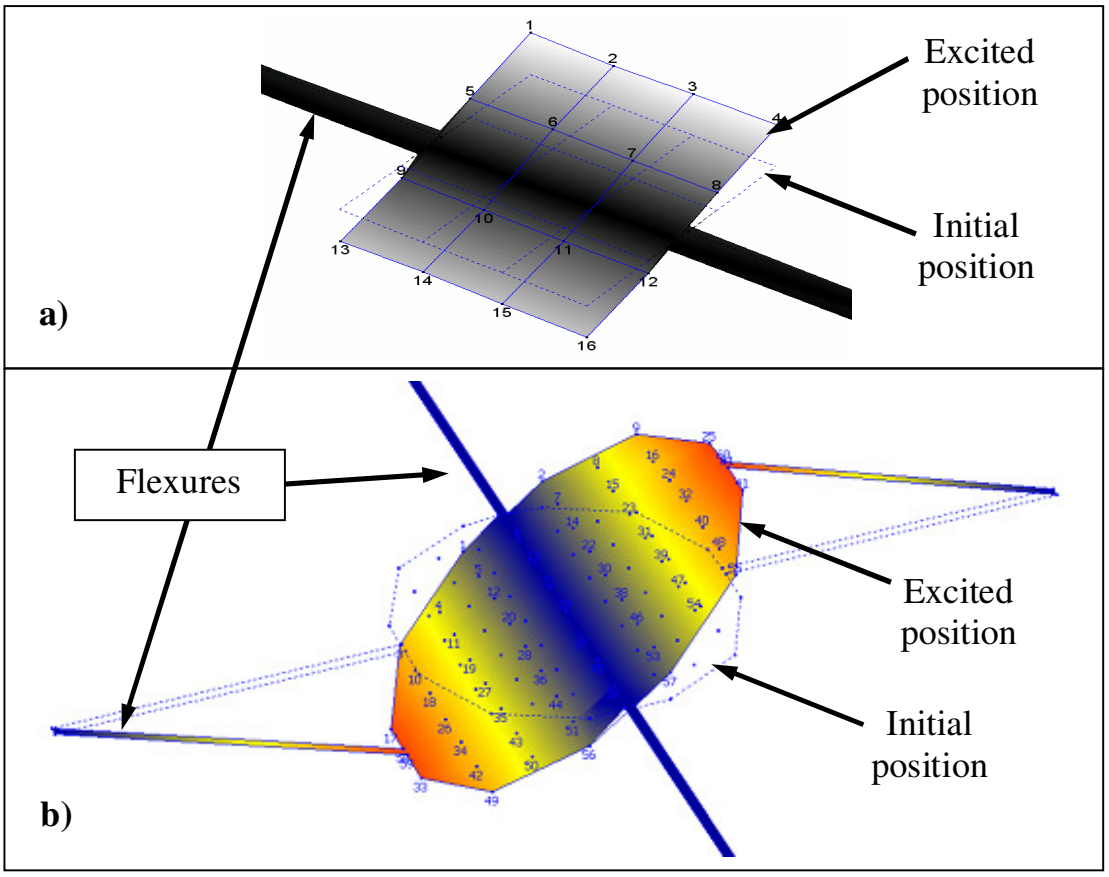

Figure 4.6: ME'Scope torsional mode representation of (a) electromagnetic scanner, (b) electrostatic scanner (ME'Scope)

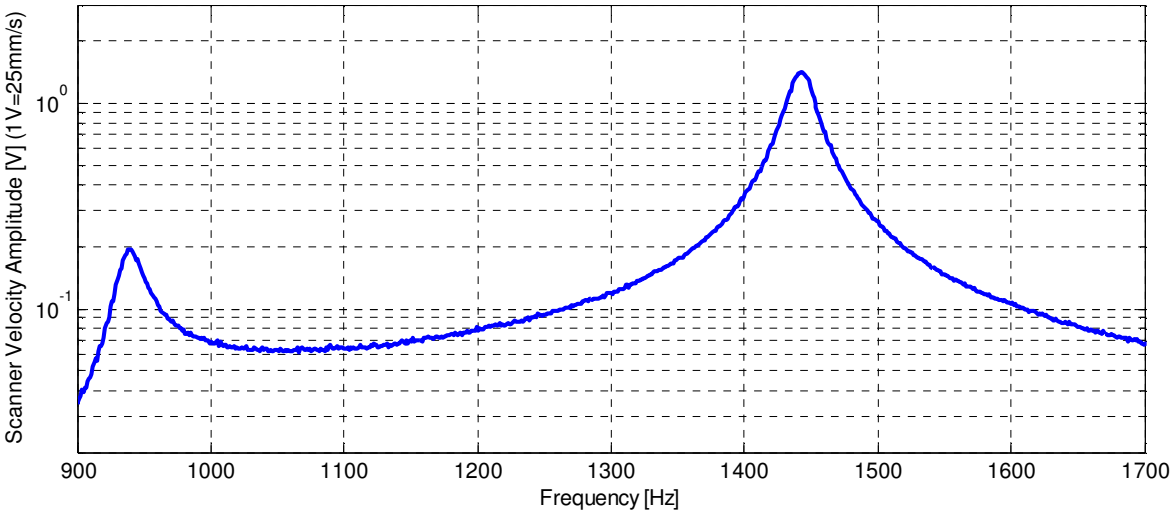

Figure 4.7: Frequency response function of the electromagnetic scanner
(Point 1, under 40mV sinusoidal input excitation)

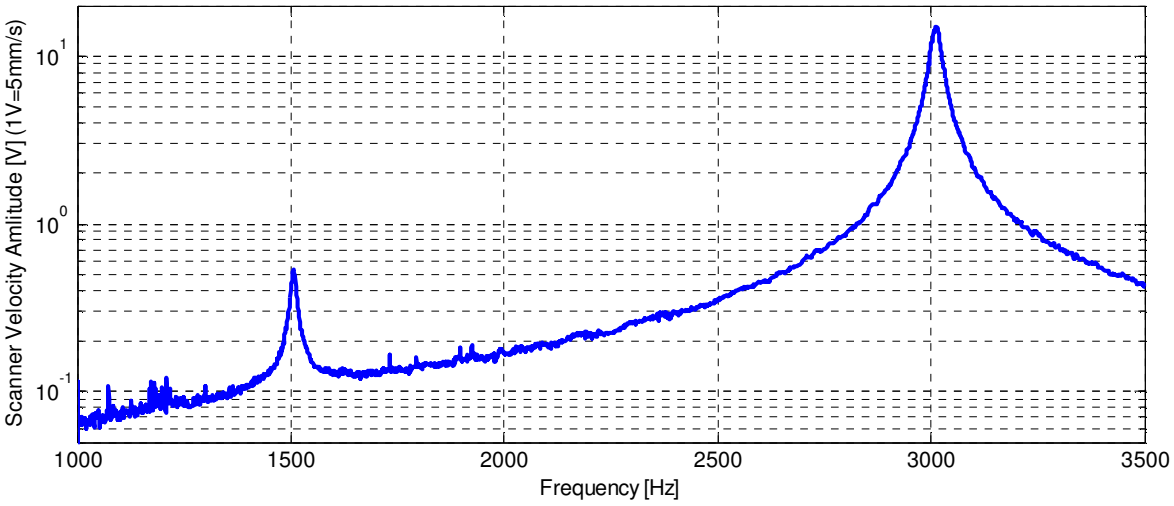

Figure 4.8: Frequency response function of the electrostatic scanner
(Point 17, under 1V sinusoidal input excitation with 2V DC offset)

The real time feedback process can only be achieved by measurement of one point at a time. Even though the amplitude and phase information can differ for each point, the

dynamical characteristics like the natural frequency (ω_n), the quality factor (Q) and the time constant (τ) will be calculated from the FRF of one measurement point only, as they do not depend on the measurement location. In addition, since the quality factors of the systems are high enough, the natural frequencies will be taken equal to the damped natural frequencies of the corresponding resonance peaks.

4.3 Velocity Feedback

To observe the effect of the change in velocity gain G to the dynamical characteristics, frequency response curves for discrete G values are plotted for the electromagnetic and electrostatic scanners (see Figures 4.9 and 4.10, respectively). The quality factors and time constants are calculated from the receptance graphs (displacement per input excitation) and their percent changes with respect to G are plotted for the electrostatic scanner in Figure 4.11. As seen from the plots, Q and τ are increasing with increasing G, while G barely has an effect on the resonance frequency, as expected from Equations 2.18-2.20.

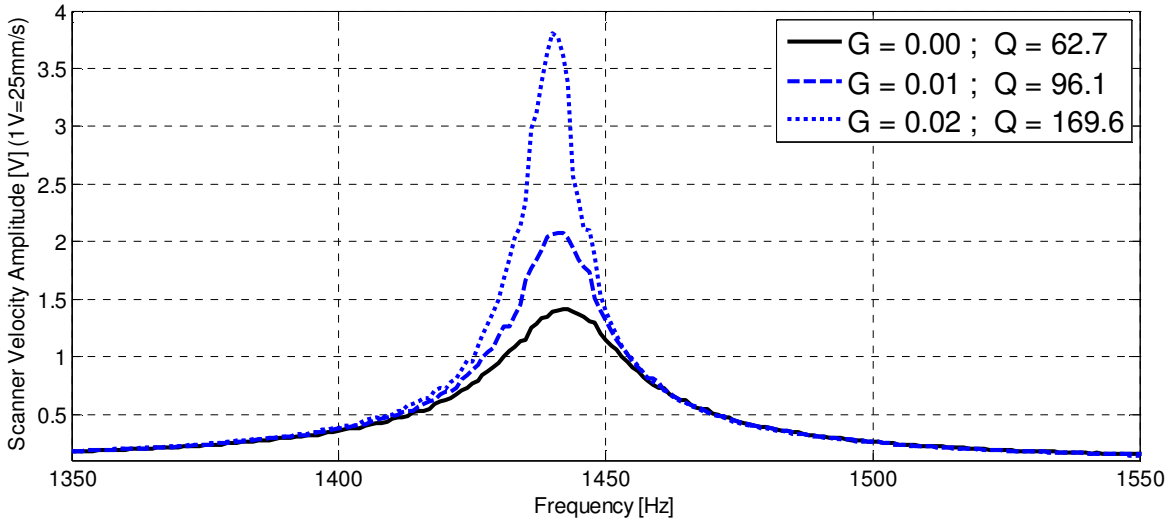

Figure 4.9: Frequency response functions for different G values
(Electromagnetic scanner, under 40mV sinusoidal input excitation)

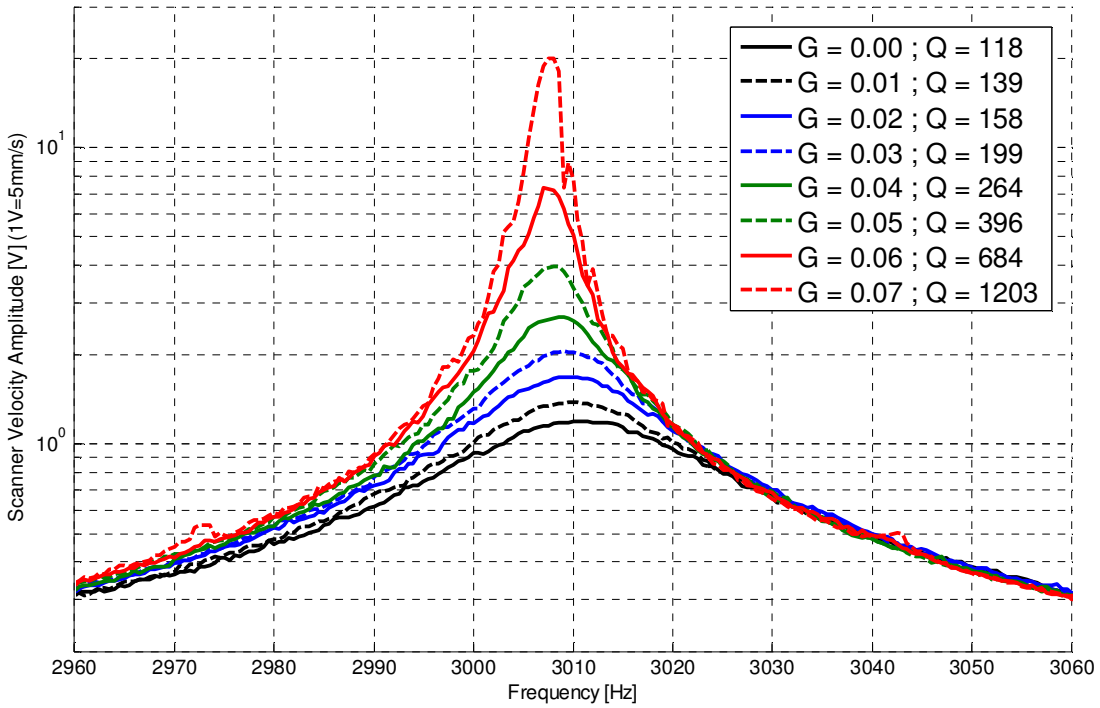

Figure 4.10: Experimental frequency response functions for different G values (Electrostatic scanner, under 80mV sinusoidal input excitation)

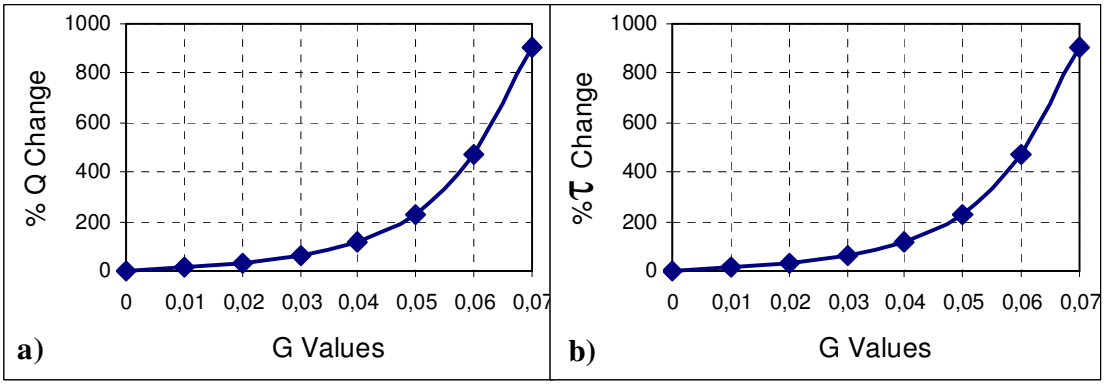

Figure 4.11: Percent change in (a) quality factor, (b) time constant, for different G values on the electrostatic scanner.

The electromagnetic scanner becomes unstable at a maximum G value of 0.026. One should also notice the fluctuation on the right fall of the curve with gain G=0.07 where the electrostatic scanner starts to undergo the unstable regime. Beyond that velocity gain G, for

instance for G=0.071, the system becomes unstable. The quality factor of the electrostatic scanner could be increased by a factor of approximately 10, while the electromagnetic scanner's quality factor is increased to only 3 times the initial value.

4.4 Position Feedback

Similarly, to see the influence of the position gain H, frequency response curves under different H gain voltages are plotted. As one can notice, the voltages required for significant position feedbacks are more than required for the velocity feedbacks. Because of the voltage limitations of the electromagnetic scanner (see Figure 4.1), the position feedback was not successful. The reasons will be discussed in Chapter 5. Hence, only the electrostatic scanner results for position feedback are plotted (see Figure 4.12).

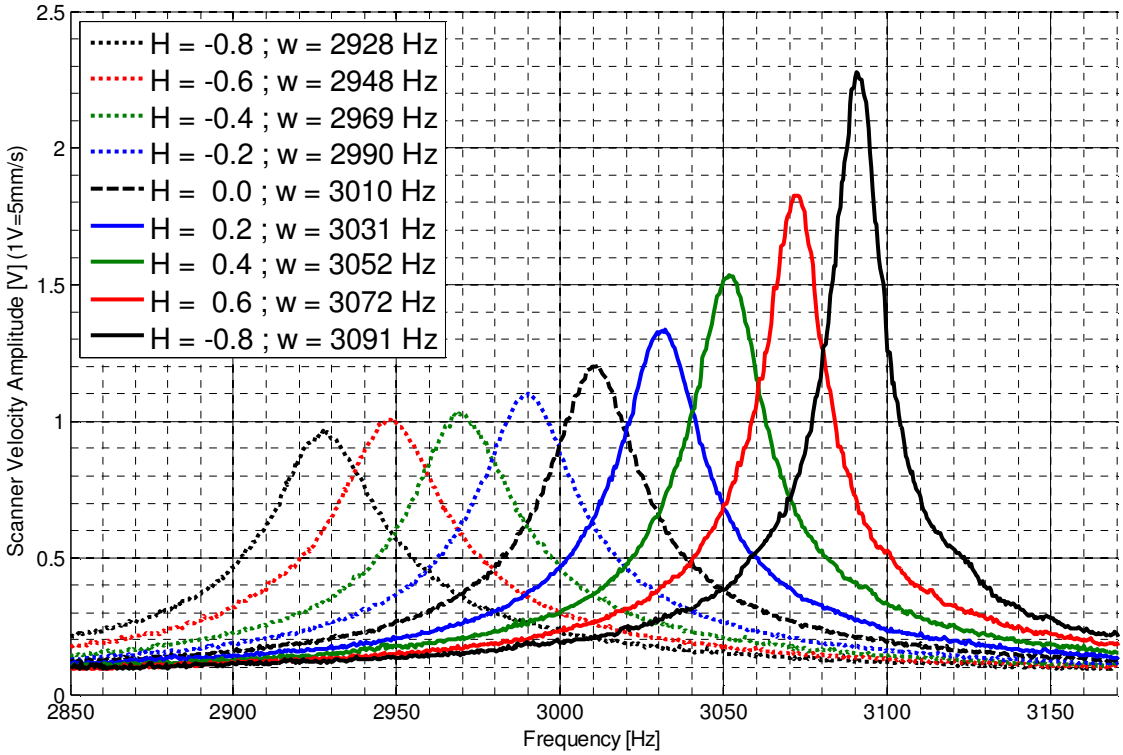

Figure 4.12: Experimental frequency response functions for different H values (Electrostatic scanner, under 80mV sinusoidal input excitation)

After the quality factors and time constants are calculated again from the receptance graphs, their percent changes and the frequency shifts with respect to H are plotted in Figure 4.13. Recalling from the theory described in Section 2.5, for a second order system under pure position feedback, as long as only the stiffness is affected, the time constant should remain constant and the quality factor should stay linearly proportional with the natural frequency. However, the system does not behave as a second order system under position feedback. As seen from the plots, the time constant is increasing with increasing H gain. Moreover, while the resonance frequency shifts almost linearly with the H gain, the quality factor's increase is not linear because of the change in the time constant. This unexpected phenomenon can be explained by the frequency change of all other modes, forcing the scanner not to act as a second order system. These results will be taken into consideration in the simulation part.

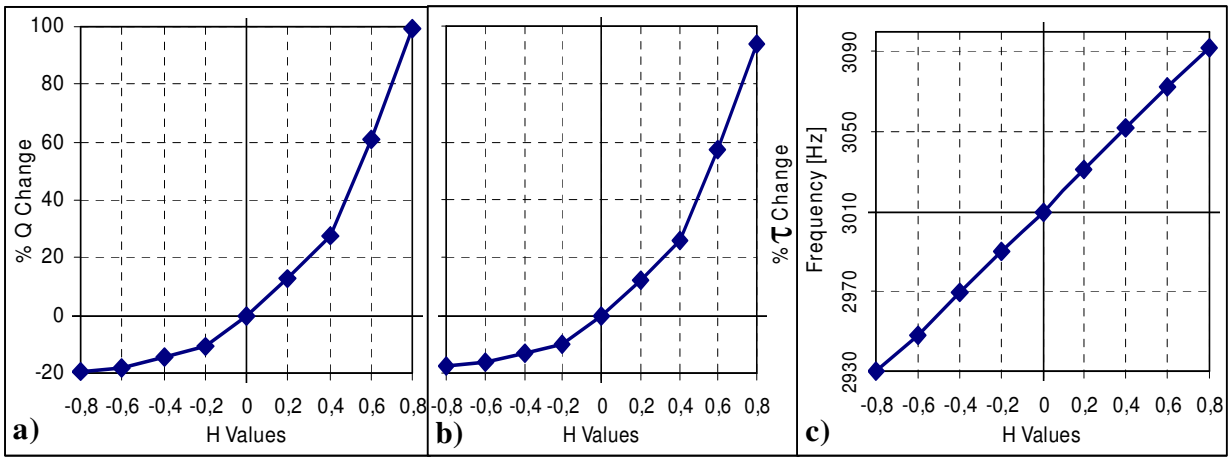

Figure 4.13: Percent change in (a) quality factor, (b) time constant and (c) the shift in resonance frequency, for different H values

4.5 Concurrent Feedback

To see the feasibility of concurrent feedback, both velocity and position feedbacks are introduced into the system together. It is demonstrated that by adjusting the gains independently, it is possible to carry the resonance to a desired frequency and change the damping of the system simultaneously (see Figure 4.14)

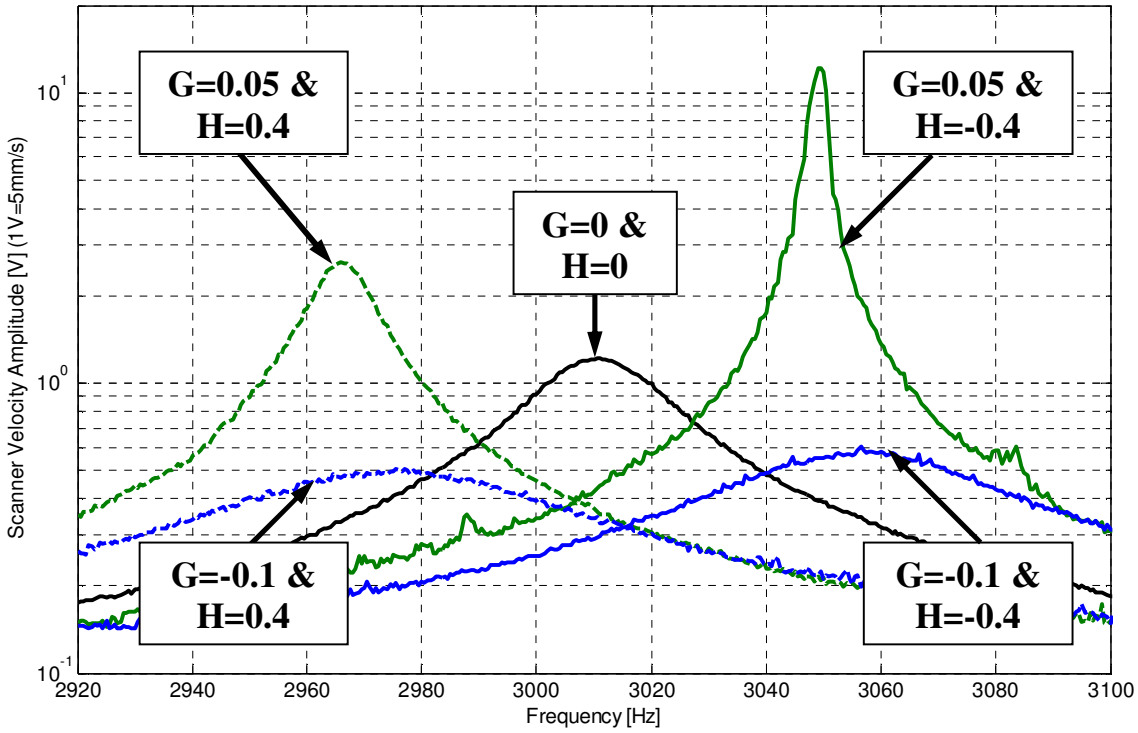

Figure 4.14: Concurrent feedback results for the electrostatic scanner

4.6 Stability Analysis From FRFs

The system under velocity feedback can be represented as in Figure 4.15, where G is the velocity gain and T(s) is the open-loop transfer function between the input voltage 'inp(s)'and the output velocity voltage 'out(s)' (see Equation 4.4). Frequency response functions are obtained by the steady-state response of the system at discrete frequency values and are used to represent the transfer function describing the sinusoidal steady-state behavior. To convert the system into frequency domain, s is replaced with the complex variable iω (see Equation 4.5).

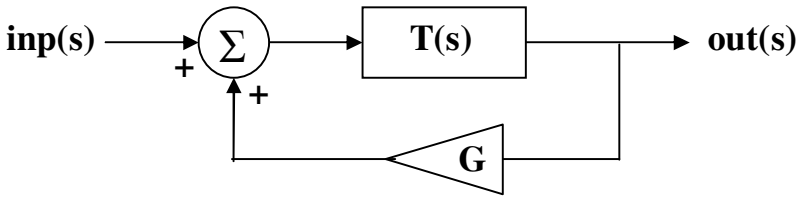

Figure 4.15: Velocity feedback block diagram

$$T(s) = \left.\frac{out(s)}{inp(s)}\right|_{G=0} \tag{4.4}$$

$$T(i\omega) = \left.\frac{out(i\omega)}{inp(i\omega)}\right|_{G=0} = \left.\frac{|out(\omega)|.e^{i\phi_{out}(\omega)}}{|inp(\omega)|.e^{i\phi_{inp}(\omega)}}\right|_{G=0} \tag{4.5}$$

$$\frac{out(i\omega)}{inp(i\omega)} = \frac{T(i\omega)}{1 - T(i\omega).G} \tag{4.6}$$

According to the closed loop transfer function, we require T(iω).G < 1 for the stability (see Equation 4.6). The G gain values where the system becomes unstable change with the frequency. Hence, to find the maximum gain value safely applicable to the system for all frequencies, the minimum possible gain should be selected. Since T(iω) and G are

inversely proportional, the critical G value can be attained at the resonance frequency, where T(iω) is at its maximum. At the resonance frequency, the phase difference between the input and output voltage is an integer multiple of 180 degrees by definition. Knowing that the phase of the input signal must be 0º, the maximum gain value is found to be the magnitude ratio of the input to the output at the resonance frequency (see Equations 4.7-4.9).

$$\phi_{inp(\omega)} = 0° \rightarrow e^{i\phi_{inp(\omega)}} = 1 \tag{4.7}$$

$$\phi_{out(\omega_N)} = n.180° \rightarrow e^{i\phi_{out(\omega_N)}} = (-1)^n \tag{4.8}$$

$$G < \frac{1}{T(i\omega_N)} = \frac{|inp(\omega_N)|.e^{i\phi_{inp}(\omega_N)}}{|out(\omega_N)|.e^{i\phi_{out}(\omega_N)}} = (-1)^n.\frac{|inp(\omega_N)|}{|out(\omega_N)|} \tag{4.9}$$

From Equation 4.9, the maximum gain values for the electromagnetic and electrostatic scanners are found $G_{max,EM}$ = (40mV)/(1.4V) = 0.029 and $G_{max,ES}$ = (80mV)/(1.2V) = 0.067, respectively. In these cases, n is an even number for both scanners; however the velocity gain sign should be switched according to the resonance mode. The results are in accordance with the experimental gain limits ($G_{exp,EM}$ = 0.026 and $G_{exp,ES}$ = 0.071).

Chapter 5

SIMULATION RESULTS & COMPARISON

In this section, Simulink models of the scanners and the feedback loops are developed to verify the experimental measurements. The effect of velocity and position feedback loops on the dynamical behavior of the scanners is further investigated.

5.1 Construction of the Simulation Model

Several curve fitting methods are used in order to have an accurate representation of the scanner system. These methods, being second order fit, "*invfreqs*" function fit and a superposition fit, are explained in the following sections (see Appendix C for the MATLAB code).

5.1.1 2nd Order Function Fit

The simplest method is to apply a second order system with a constant phase delay. This approach could not always fit a proper curve to the experimental data because of the effects of the other resonant peaks, as mentioned in the previous chapter. The more the resonance frequencies are apart, the less their influences become on each other. Therefore, in order to represent the system as a second order system, the working resonance peak (the second resonance peak, in our study) should be sufficiently separated from adjacent resonance peaks. It can be observed from Figure 5.1 that the second order fit is not reliable since it is not possible to overlap the curves at the frequencies away from the working resonance peak.

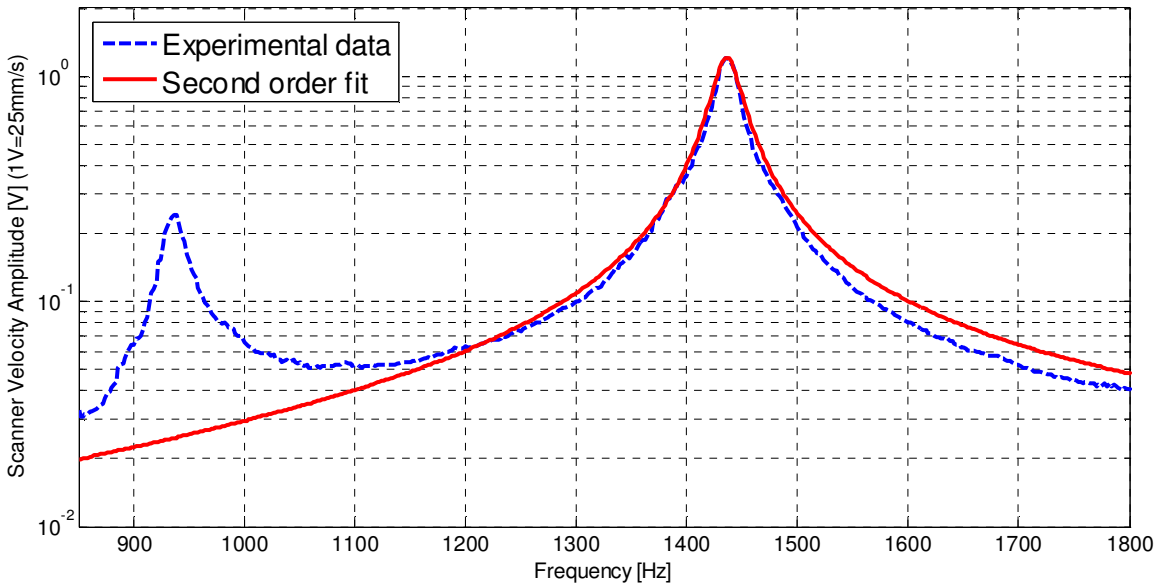

Figure 5.1: 2nd order function fit to the experimental data of the electromagnetic scanner under 40mV sinusoidal input voltage

5.1.2 Invfreqs Function Fit

To fit a better curve to the system, a wider frequency range is taken into consideration covering the first two resonant peaks. Over this frequency range, the "*invfreqs*" function of MATLAB, which is an analog filter least squares fit to the frequency response data, is used. The function requires both the experimentally collected amplitude and phase data for curve fitting operation. The order of the function is set manually. Lower orders were insufficient to duplicate the frequency response function. On the other hand, higher degree polynomials could be applied to diminish the error between experimental data and the simulation. However, it should be kept in mind that the measurement data is always noisy and imperfect. Therefore, trying to fit higher order polynomials will eventually result in producing non-existent behaviors, rather than reducing the simulation error. Eventually, an optimum transfer function between the input voltage signal and output velocity of the

scanner, having 3rd and 6th order polynomials in the numerator and denominator respectively, yielded satisfactory results, as shown in Figure 5.2.

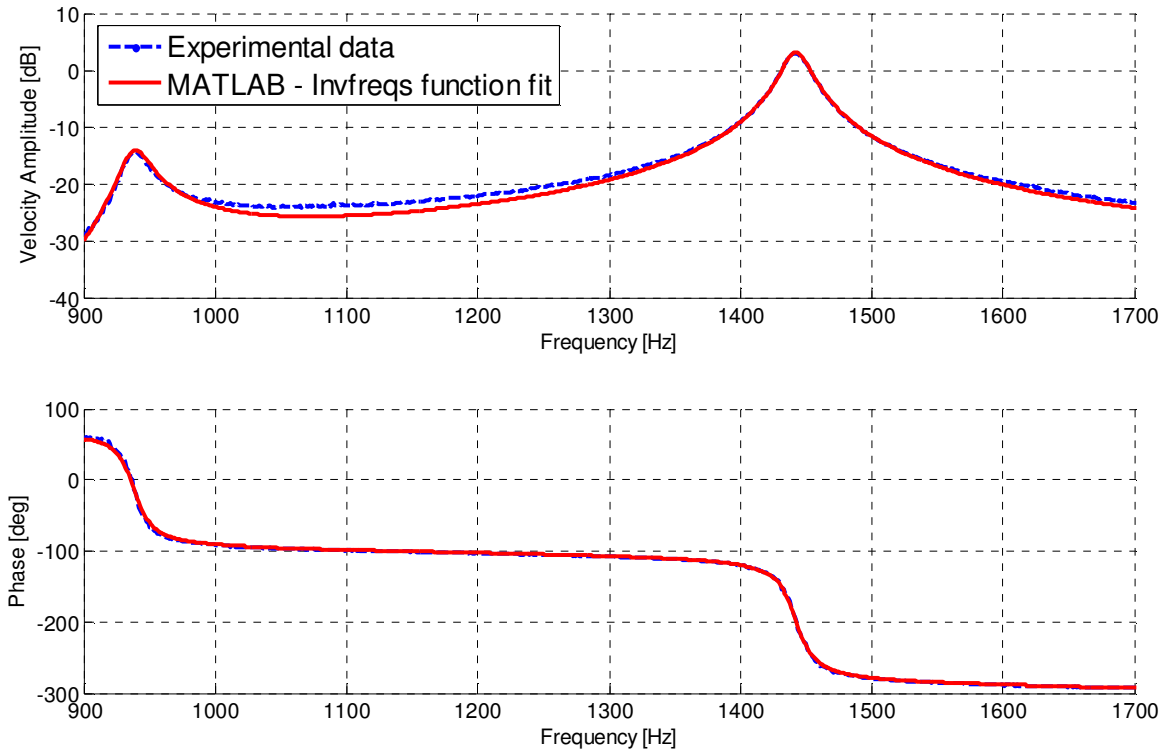

Figure 5.2: MATLAB Invfreqs function fit to the experimental data of the electromagnetic scanner under 40mV sinusoidal input voltage

5.1.3 Superposition of Systems

The previous fit was satisfactory but it required clean phase information. Both to dispose of the phase data necessity and to have a control over the transfer function variables, modeling the system as a combination of several systems is preferred. The transfer function is constructed by the superposition of two second order polynomials (one for each resonance frequency), a delay and a correcting function and a scaling factor. After the resonance frequencies of the scanners (ω_1=939 Hz and ω_2=1442 Hz for electromagnetic

scanner, ω_1=1507 Hz and ω_2=3010 Hz for the electrostatic scanner) are obtained from the amplitude plots and the quality factors are calculated using the half-power method around the resonance peaks, the 1st and 2nd order terms of the polynomials are calculated using the corresponding peak's dynamical characteristics. As can be seen from figure 5.3, the series connection of only these second order systems needs some corrections to properly fit the experimental amplitude and phase data. The correcting function is introduced and the amplitudes are scaled to overlap the resonance peaks. Subsequent to the conformity of the amplitude curves, this transfer function is introduced a constant delay to form the final transfer function, which also gave satisfactory results for both amplitude and phase data, as shown in figure 5.4. The electrostatic scanner's ultimate transfer function can also be seen in figure 5.5.

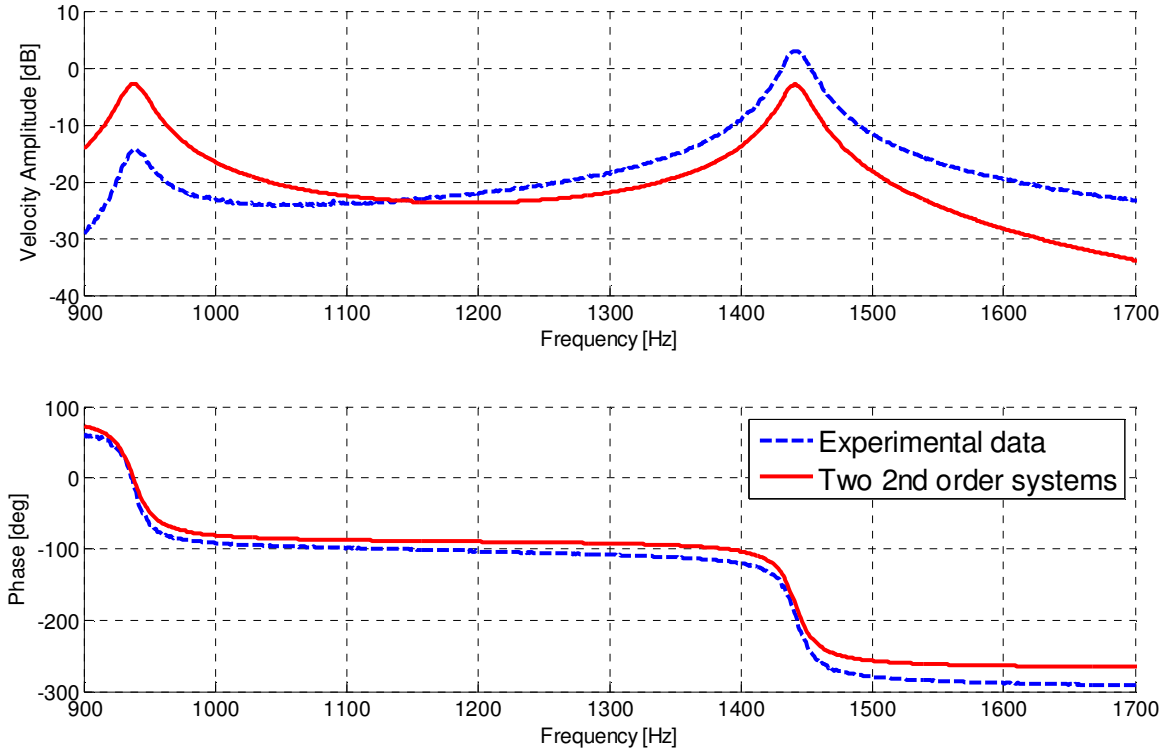

Figure 5.3: Two 2nd order systems without a scaling factor or a delay

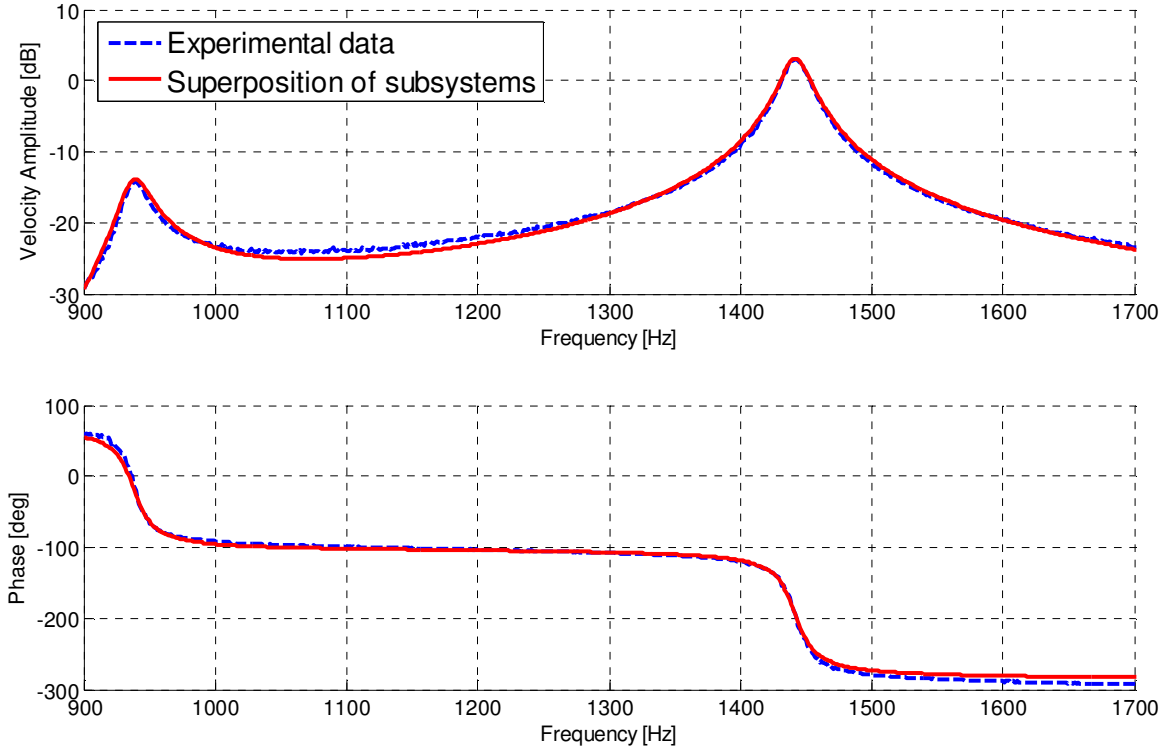

Figure 5.4: Superposition of subsystems fit to the experimental data of the electromagnetic scanner under 40mV sinusoidal input voltage

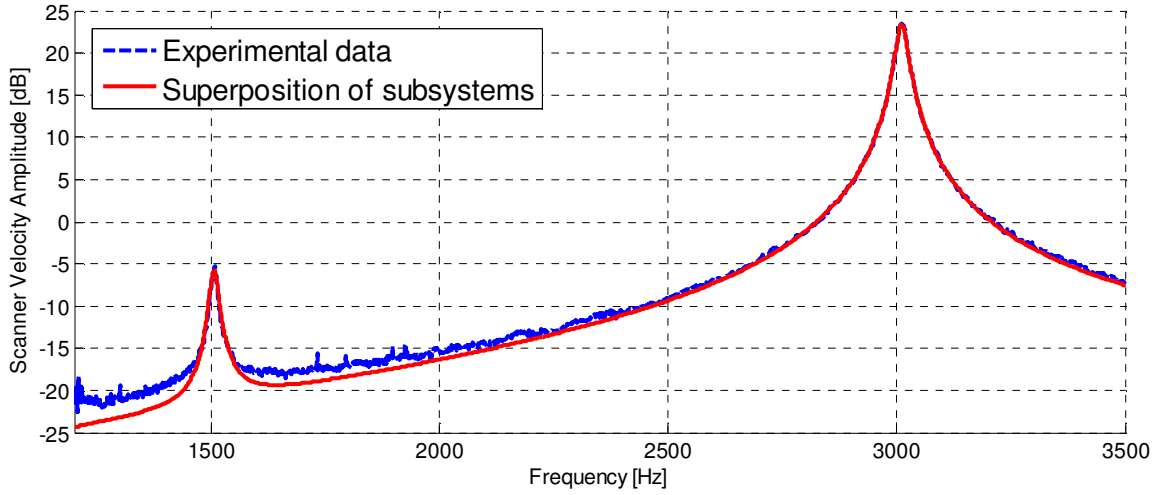

Figure 5.5: Superposition of subsystems fit to the experimental data of the electrostatic scanner under 1V sinusoidal input excitation with 2V DC offset

Successively having built the transfer functions, a SIMULINK® model of the scanners with feedback loops is developed to justify the consistency of numerical approach with experimental measurements exposed to feedback gains. The next step is to change the velocity and position gains, G and H, in the SIMULINK® model to further investigate the effect of feedbacks gains on the dynamical characteristics of the scanners (see Figure 5.6) (see Appendix D for the MATLAB code).

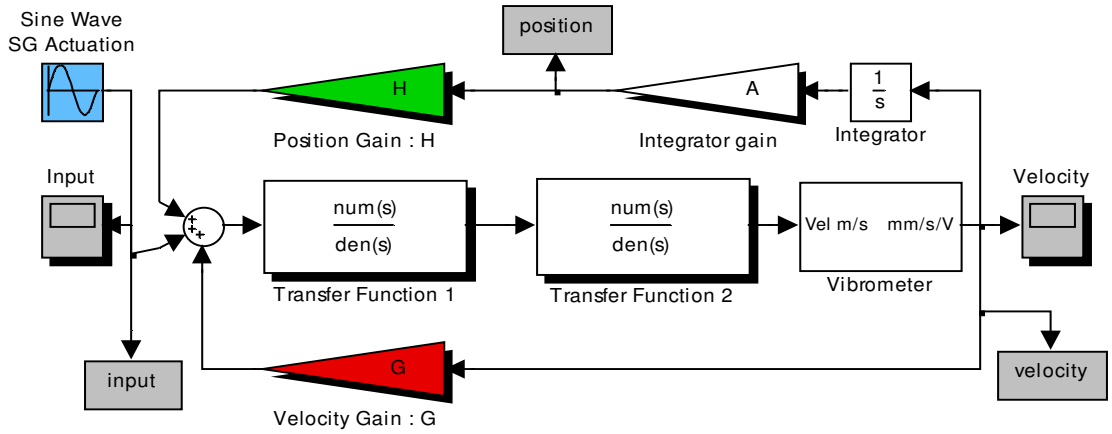

Figure 5.6: SIMULINK Model with feedback loops

5.2 Velocity Feedback Comparison

As shown in Figures 5.7 and 5.8, the response of the numerical models is very close to experimental data for different gain values. It should be recalled that the resonance frequencies under pure velocity feedback must remain unchanged, as in the case with simulation curves. Yet, slight shifts in the experimental resonance peaks are noticed for increasing G values (3 Hz maximum). In spite of the fact that there are small discrepancies due to that shift, the curves are reasonable even for greater values of G gains. For magnetic and electrostatic scanners, the curves are plotted up to G_{EM}=0.02 and G_{ES}=0.06, since the superposition simulation results show that the systems become unstable at G_{EM}=0.029 and G_{ES}=0.067, respectively, which are also in accordance with the theoretical stability limits (for 2nd order fit: G_{EM}=0.028 and G_{ES}=0.067, for invfreqs fit: G_{EM}=0.029 and G_{ES}=0.067).

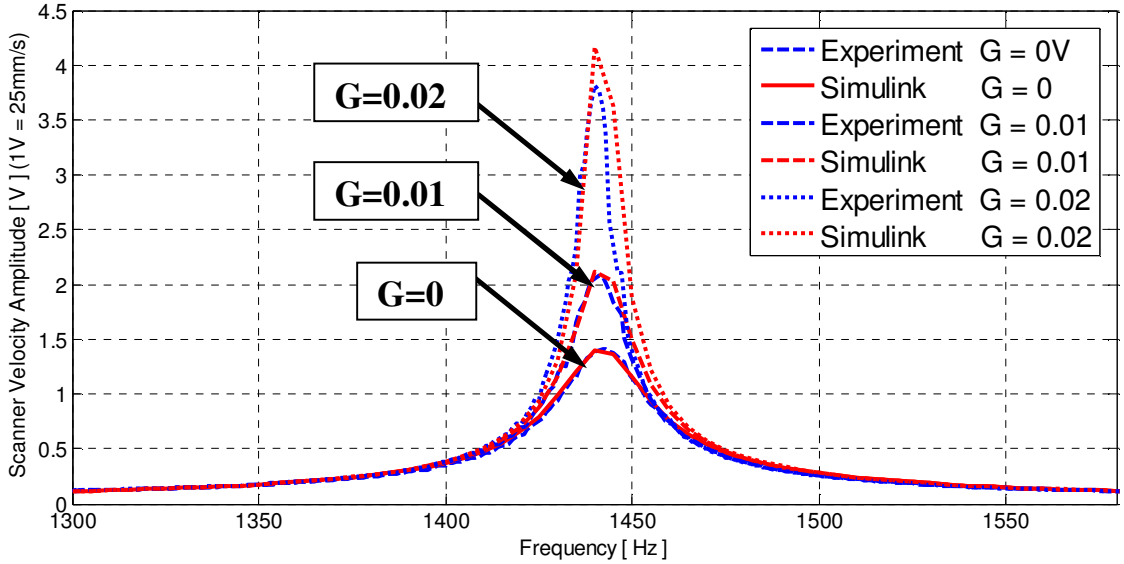

Figure 5.7: Electromagnetic scanner velocity feedback comparison

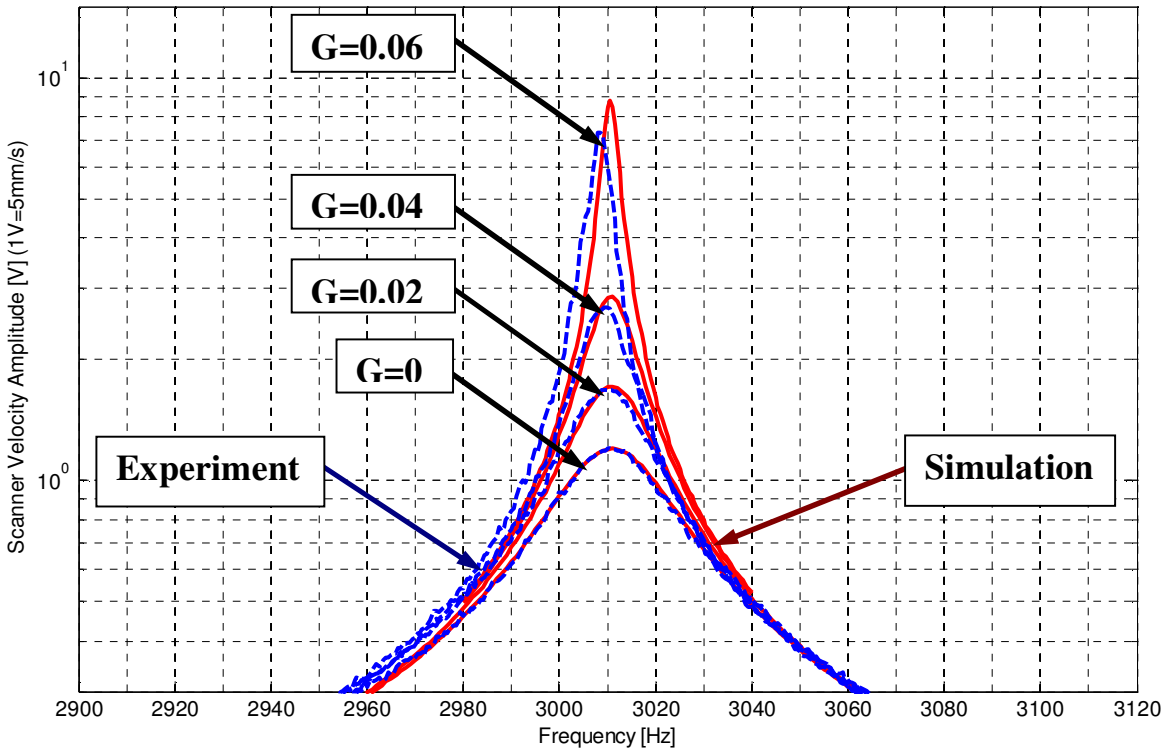

Figure 5.8: Electrostatic scanner velocity feedback comparison

5.3 Position Feedback Comparison

Having obtained the simulation position feedback curves for both scanners, comparison with the experimental data is made for only the electrostatic scanner. To understand why a position feedback did not work for the electromagnetic scanner, we looked at the resonance frequency changes per position feedback gains ($d\omega/dH$). Approximate values for the electromagnetic and the electrostatic scanner are $(d\omega/dH)_{EM}$ = 40Hz (4Hz/1V) and $(d\omega/dH)_{ES}$ = 100Hz (10Hz/1V), respectively. While it is possible to introduce the electrostatic scanner a voltage of 8 volts to shift the resonance frequency by 80Hz, the maximum possible voltage for the electromagnetic scanner is 200-250mV, which corresponds to a frequency shift of only 1Hz. Although there is no theoretical stability limit for the position feedback (except from reaching 0Hz), it may not be applicable for some systems due to voltage limitations mentioned earlier.

Even though a position feedback could not be achieved for the electromagnetic scanner, the simulation results provide a better understanding about the feedback response of the scanners. It is observed that the second peak's resonance frequency is decreased and the resonance curves are approaching to each other as the gain H is increased, and vice versa, for both scanners. The second important behavior to notice is that the amplitudes of approaching curves are increasing in the electromagnetic scanner, while an opposite effect is present in the electrostatic scanner (see Figures 5.9 and 5.10). Also, the reverse of this phenomena is observed in the contrariwise direction. The change in the amplitudes with altering frequency is the result of the neighboring resonance peak and the correcting function. Nevertheless, whether the peak amplitude is going to increase or decrease is related with which one of the neighboring resonance peak and the correcting function is more dominant. For example, if the neighboring resonance peak effect is more dominant when compared to the effect of the correcting function, then the peak amplitudes will increase as the peaks are approaching, as if one curve is climbing to the other curve's peak.

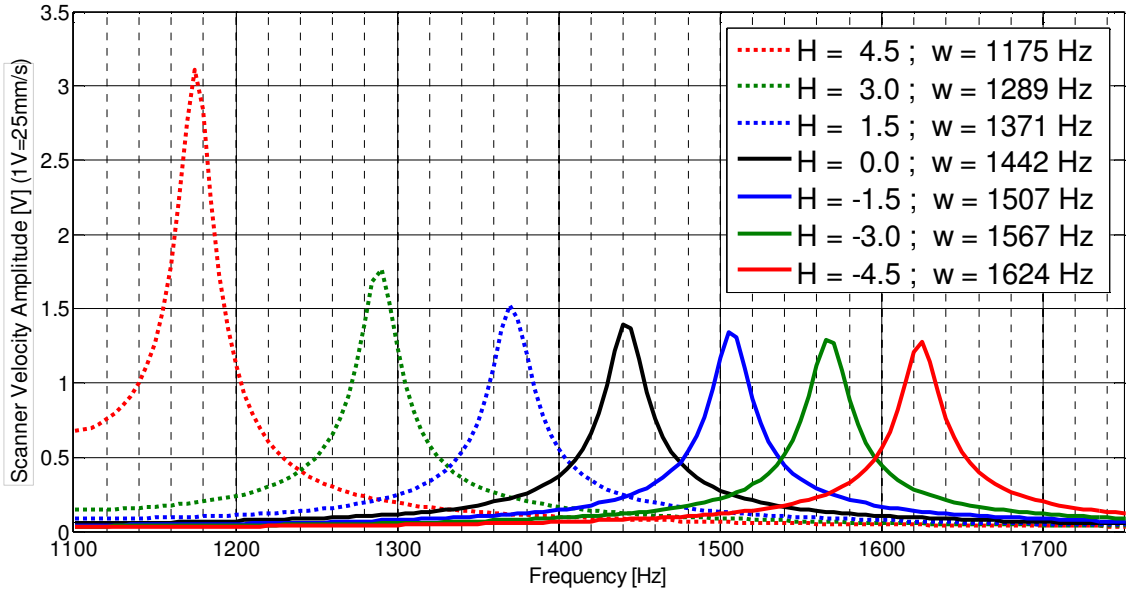

Figure 5.9: Electromagnetic Scanner Position Feedback Curves (Simulation data)

As can be seen from figure 5.10, the simulation results differ from the experimental ones in terms of amplitudes while the frequency shifts are in accordance. This may again be the consequence of other system dynamics. Recall that the simulation is based on the superposition of mainly two resonance peaks. However, there are countless resonance frequencies in the real system, which are not feasible to simulate. Since the velocity feedback alone has no influence on the frequency, the simulation and experimental results are in agreement. In case of position feedback though, the resonance frequency variations affect the amplitudes unpredictably.

Another factor may be that the resistance values in the feedback circuit are selected just for the original resonance frequency. As the resonance frequency shifts, the phase difference in the phase shifter and the integrator gain value in the integrator slightly diverge from the intentional values they should be. However, this kind of divergence can not be an issue in the simulation, causing a difference from the experiments.

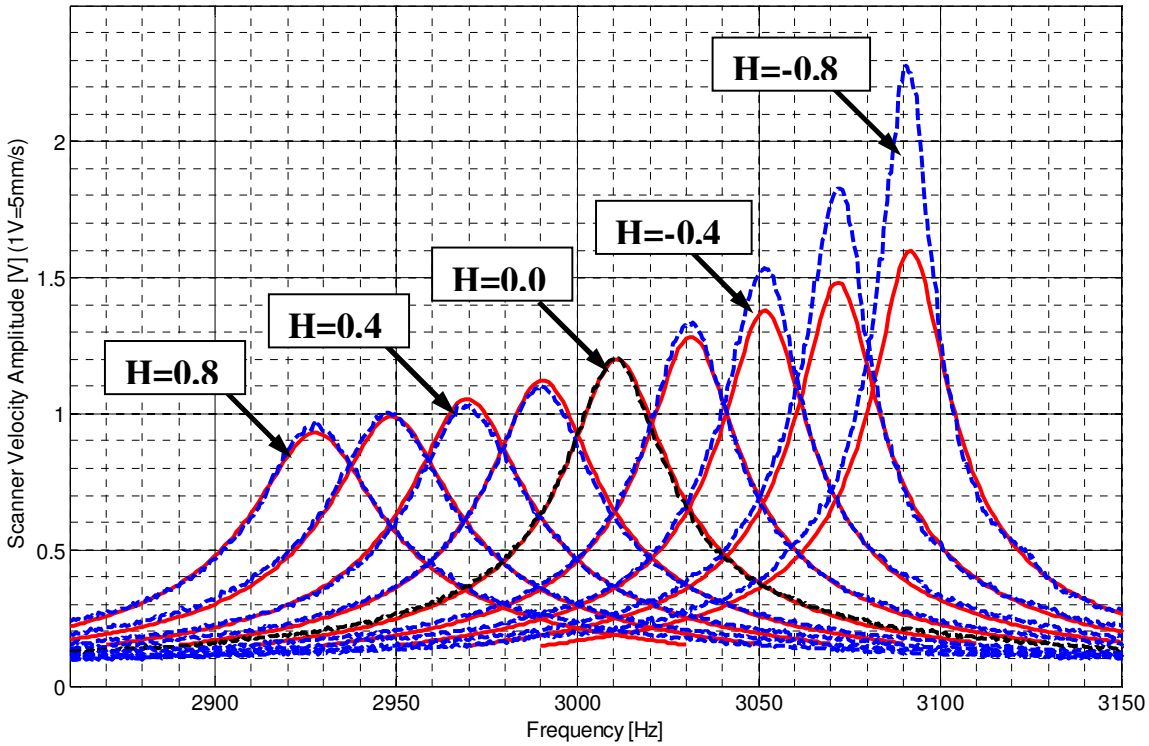

Figure 5.10: Electrostatic Scanner Position Feedback Curves

(Blue dashed lines: Experimental data, Red solid lines: Simulation data)

5.4. Concurrent Feedback and Dynamic Characteristics Analysis

The advantage of having two feedback loops is that once the resonance frequency is set, the effective damping of the system can be altered independently by adjusting the gain G. By adjusting both the position and velocity gains, the resonance frequency and the damping characteristics of the system were proven to be set simultaneously. Because of the fact that there are slight frequency shifts in the experimental velocity feedbacks, the simulation results are no flawless match. Still, the system tendencies under concurrent feedback are considerably similar (see Figure 5.11).

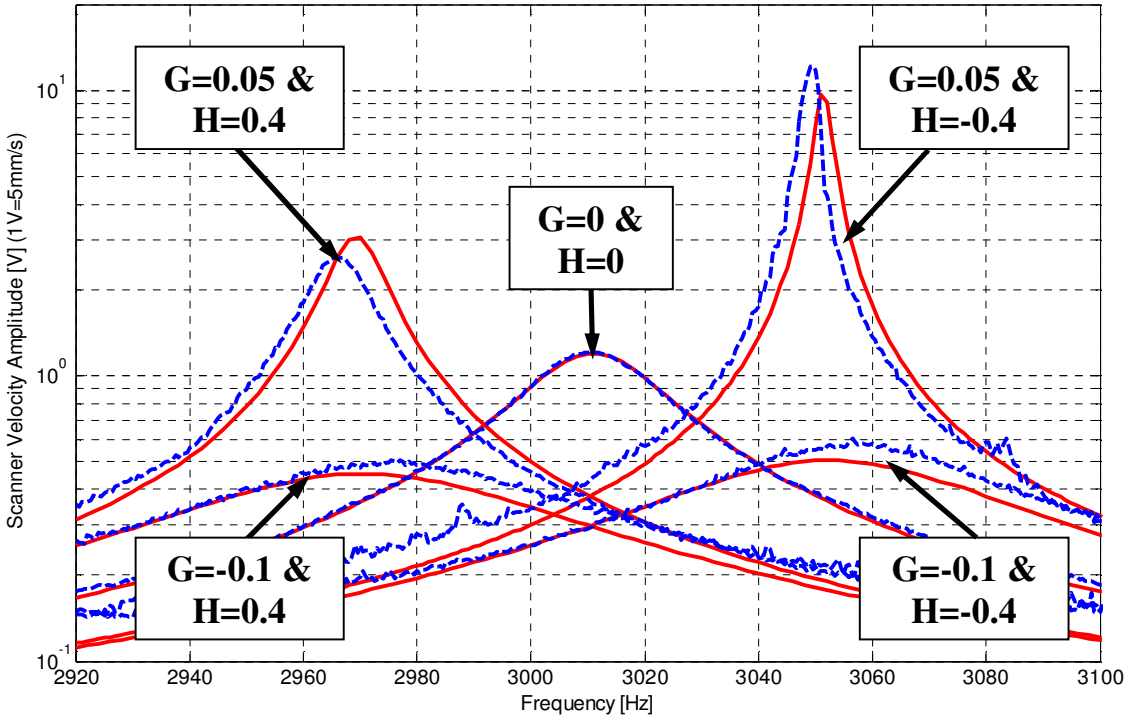

Figure 5.11: Electrostatic Scanner Concurrent Feedback Results

(Blue dashed lines: Experimental data, Red solid lines: Simulation data)

To see the percent changes in quality factor and time constant, a list of test cases altering G and H gains is tabulated (see Tables 5.1 and 5.2). One can notice from the Tables that changing the gain G has a major influence on both quality factor and time constant, while it has no influence on any of the resonance frequencies which are altered by H gains. Unfortunately, there is always a trade-off between quality factor and the time constant. Even though there are some regions where both the quality factor and the time constant are improved, their percent changes are extremely insignificant. Considering this fact, the gain G has to be adjusted depending on the application priorities. In stability limits of the electrostatic scanner, a quality factor improvement of almost 2400% or a decrease in settling time by 60% is observed.

Due to the coupling of vibration modes, the alterations in the gain H have an influence on every system characteristics, in some degree. For greater G gains, remarkable changes are observed in quality factor and time constant, along with the change of the H gains. As G gains decrease, especially for its negative values, the influence of H gains over damping characteristics become insignificant. Meanwhile, the resonance shifts stays generally linear with H and are independent of G. Therefore, it is important to set the working frequency prior to the adjustment of G gains.

Table 5.1: Percent changes in peak amplitude, quality factor and time constant for different values of G & H gains for the electromagnetic scanner.

	H	3.0	1.5	0	-1.5	-3.0	-4.5
G	Freq [Hz]	1289	1371	1442	1507	1567	1624
0.02	Vmax [V]	10.80	6.48	4.86	4.17	3.79	3.59
	% dQ	695.1	316.4	249.2	208.2	195.1	209.5
	% dτ	790.1	338.0	249.2	194.9	171.5	174.8
0.01	Vmax [V]	3.19	2.47	2.19	2.04	1.94	1.88
	% dQ	69.7	60.5	57.5	59.3	60.5	65.4
	% dτ	90.0	68.8	57.5	52.5	47.7	46.9
0	Vmax [V]	1.77	1.53	**1.42**	1.35	1.31	1.28
	% dQ	-4.9	-1.5	**0.0**	4.3	7.9	11.5
	% dτ	6.5	3.6	**0.0**	-0.2	-0.7	-1.0
-0.01	Vmax [V]	1.23	1.11	1.05	1.01	0.99	0.97
	% dQ	-33.6	-28.5	-25.1	-20.8	-17.2	-14.6
	% dτ	-25.7	-24.8	-25.1	-24.2	-23.8	-24.2
-0.02	Vmax [V]	0.94	0.87	0.83	0.81	0.79	0.78
	% dQ	-49.2	-43.9	-40.2	-36.7	-33.4	-31.6
	% dτ	-43.1	-41.0	-40.2	-39.5	-38.8	-39.3
-0.03	Vmax [V]	0.76	0.71	0.69	0.67	0.66	0.65
	% dQ	-59.2	-54.1	-50.2	-47.2	-44.9	-42.6
	% dτ	-54.3	-51.7	-50.2	-49.5	-49.3	-49.1

Table 5.2: Percent changes in peak amplitude, quality factor and time constant for different values of G & H gains for the electrostatic scanner.

G	H	0.8	0.6	0.4	0.2	0	-0.2	-0.4	-0.6	-0.8
	Freq [Hz]	2928	2949	2970	2991	3011	3032	3052	3072	3092
0.06	Vmax [V]	3.07	3.82	4.99	7.08	11.18	33.72	-	-	-
	%ΔQ	150.3	210.5	307.0	484.3	781.4	2393	-	-	-
	%Δτ	157.4	217.1	312.7	488.2	781.4	2376	-	-	-
0.04	Vmax [V]	1.74	1.95	2.22	2.56	2.99	3.58	4.40	5.65	7.83
	%ΔQ	41.2	60.1	83.2	113.4	150.0	197.5	266.0	373.7	551.2
	%Δτ	45.3	63.5	85.7	114.9	150.0	195.5	261.1	364.3	534.1
0.02	Vmax [V]	1.21	1.31	1.43	1.56	1.71	1.89	2.10	2.35	2.66
	%ΔQ	-1.6	7.4	17.6	29.8	42.9	57.7	76.9	101.0	128.2
	%Δτ	1.2	9.7	19.3	30.7	42.9	56.6	74.5	97.0	122.2
0	Vmax [V]	0.93	0.99	1.05	1.12	**1.20**	1.28	1.38	1.48	1.60
	%ΔQ	-24.5	-19.2	-13.4	-7.1	**0.0**	7.7	16.6	26.3	30.9
	%Δτ	-22.4	-17.5	-12.2	-6.5	**0.0**	7.0	15.0	23.8	27.5
-0.02	Vmax [V]	0.76	0.79	0.83	0.88	0.92	0.97	1.03	1.08	1.14
	%ΔQ	-38.6	-35.1	-31.3	-27.2	-22.8	-18.2	-13.0	-7.6	-1.8
	%Δτ	-36.9	-33.7	-30.3	-26.8	-22.8	-18.8	-14.2	-9.4	-4.4
-0.04	Vmax [V]	0.64	0.66	0.69	0.72	0.75	0.78	0.82	0.85	0.89
	%ΔQ	-48.2	-45.6	-42.9	-40.1	-37.2	-33.9	-30.6	-27.3	-23.7
	%Δτ	-46.7	-44.4	-42.1	-39.7	-37.2	-34.3	-31.6	-28.8	-25.7
-0.06	Vmax [V]	0.55	0.57	0.59	0.61	0.63	0.65	0.68	0.70	0.73
	%ΔQ	-55.5	-53.6	-51.7	-49.7	-47.6	-44.9	-42.2	-40.0	-37.9
	%Δτ	-54.2	-52.6	-51.0	-49.3	-47.6	-45.3	-43.0	-41.2	-39.5
-0.08	Vmax [V]	0.48	0.50	0.51	0.53	0.55	0.56	0.58	0.60	0.62
	%ΔQ	-60.7	-59.3	-57.7	-56.0	-54.2	-52.4	-50.7	-49.0	-47.2
	%Δτ	-59.6	-58.4	-57.1	-55.7	-54.2	-52.7	-51.4	-50.0	-48.6
-0.10	Vmax [V]	0.43	0.44	0.45	0.47	0.48	0.49	0.51	0.52	0.53
	%ΔQ	-64.8	-63.6	-62.5	-61.2	-59.9	-58.4	-57.1	-55.8	-54.1
	%Δτ	-63.8	-62.9	-61.9	-61.0	-59.9	-58.7	-57.7	-56.7	-55.3

Chapter 6

CONCLUSION & DISCUSSION

In this thesis, the effective damping and stiffness of two distinct micro scanners are adjusted experimentally using a feedback circuit. SIMULINK® models of these scanners are also developed from experimental data to investigate their dynamical behavior for different position and velocity feedback gains.

In our approach, the velocity of the scanners is measured directly using a Laser Doppler Vibrometer. Obtaining the velocity signal from the measured position signal through differentiation is not preferred since the noise in the position signal is amplified in the process; instead the velocity signal is integrated and scaled to obtain a cleaner position signal. The velocity and position signals are first multiplied by separate gains and then added to the driving signal to change the effective characteristics of the micro scanner system. By this approach, whether the goal is to bring the scanner to a desired frequency or decrease the damping, the system response can be altered in real-time, which is a noteworthy feature in scanner applications requiring quick changes.

By numerical simulations performed with Simulink®, the influence of both position and velocity feedback on the resonance frequency, damping and the settling time of the scanners is investigated. In experimental settings, it is difficult to repeat an experiment under identical environmental conditions due to variations in ground vibrations,

temperature, electrical noise and electromagnetic disturbances. It is also practically not possible to exactly spot the laser on the same measurement point with preceding experiments. Moreover, even if the experimental conditions are fixed, the material properties of the scanners (e.g. friction at the hinges) may change in course of time, affecting the results of experiments adversely. All these factors make it difficult to quantitatively compare the results of experiments under different settings. However, using numerical simulations, the resonance frequency and the effective damping of the scanners are easily altered to investigate their dynamical responses. The transfer functions of the scanners were developed based on the experimental data, since the effective mass, damping and stiffness information is unknown for resonance modes. The first two vibration modes of the scanners are taken into consideration to construct their transfer functions. For each mode, a second order transfer function is used and superposed, which helped us to understand and analyze the influence of each vibration mode on the dynamical response of the scanner individually and more effectively. The final simulation model yielded consistent results with the experimental data under feedback gains, if not perfect. The small dissimilarities were acceptable when the simulation assumptions and the experimental imperfections were taken into account.

Having a numerical model of the system and feedback loops was very helpful for estimating the system behavior and the stability range of velocity gain values that can be used in the real experiments. The overall study showed that coupling effects can significantly influence the response of the scanners as the feedback gain H is altered. Due to this effect, H also manipulates the damping characteristics, in addition to the resonance frequency. In the direction where the investigated modes are decoupling, position feedback can possibly be used to obtain more clean oscillations. The effect of concurrent feedback on dynamical characteristics of the system is also analyzed. In general, the velocity gain G is the major factor that affects the quality factor and the time constant of the system. There

is a trade-off between the quality factor and the settling time, though. While decreasing values of G reduces the time constant of the system, it also reduces the quality factor, hence the amplitude of oscillations. As the gain G increases, the effect of gain H starts to increase on damping characteristics, whereas contrarily for negative G values, it has barely have an effect. Hence, since G gains has no effect on frequency and H gains have effect on both frequency and damping, the general strategy to find the required gain amounts is to adjust the resonance frequency prior to damping. Having found the gain values for a known operating state of the micro scanner though, the order of the feedbacks will not change the result.

APPENDIX A – Experimental Process Flowchart

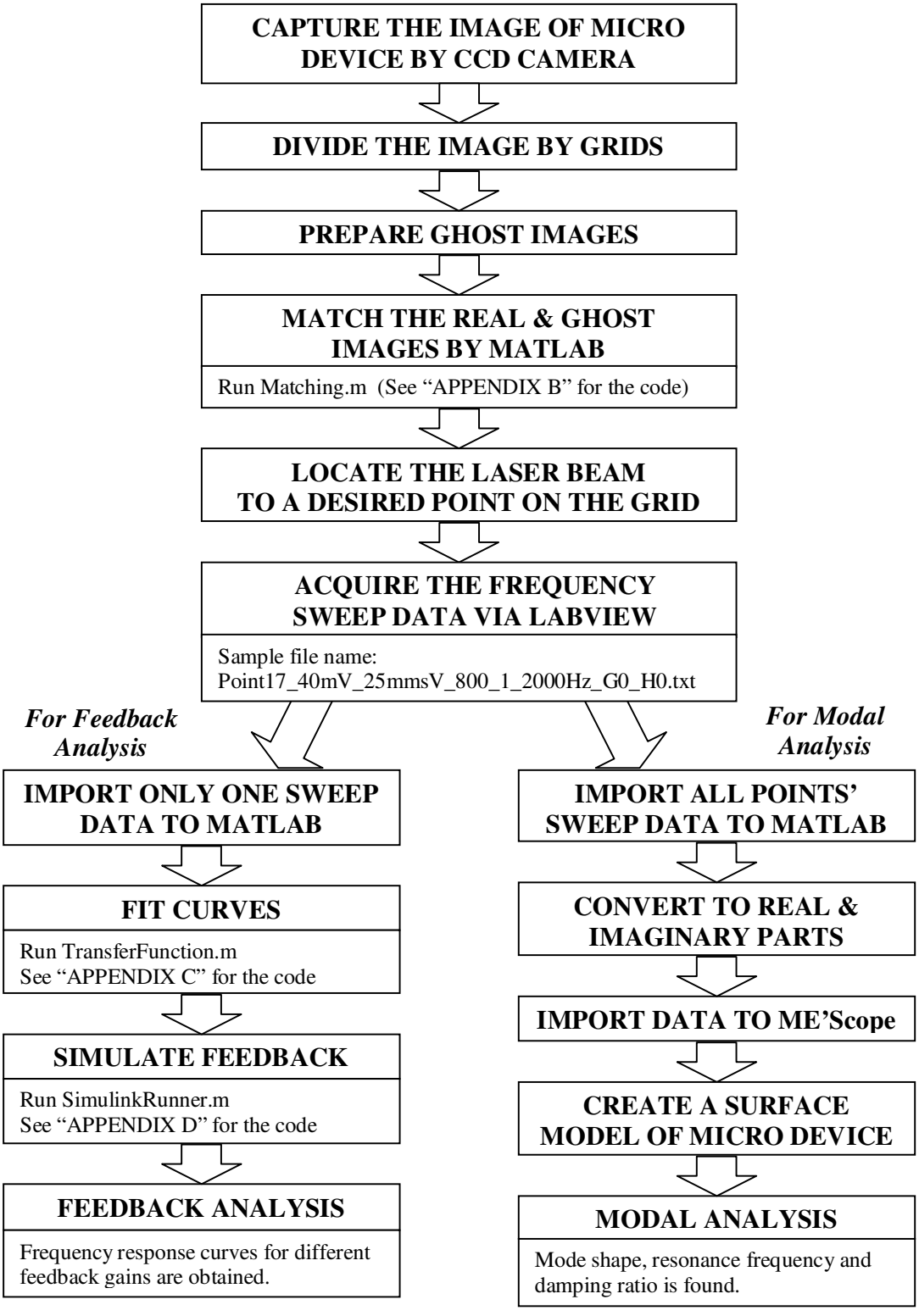

APPENDIX B – "Matching.m"

```
vid = videoinput('dcam',1,'Y8_1024x768');
grid=rgb2gray(MiddleLeft);      %Select the related portion of the image
figure();
while (1)
   f=getsnapshot(vid);
   f=(grid*0.3)+(f*0.8);        %Overlap the real CCD image and the grid image
   colormap(gray(256));
   image(f);
end
```

APPENDIX C – "TransferFunction.m"

```
clear all, close all, clc;

Measurement = importdata('Magnetic_40mV_100_1_2000hz_25mmsV_A_G00_H00.txt');

w=Measurement(:,1);   % Frequency
T=Measurement(:,2);   % Amplitude
ph=Measurement(:,3);  % Phase
db=20*log10(T);       % Amplitude in dB

UpperD=3;             % Degree of the numerator
LowerD=6;             % Degree of the denomerator

[b,a] = invfreqs(10.^(db/20).*exp(j*(ph/180*pi)),w*2*pi,UpperD,LowerD,[],70);
                      % Amplitude in normal (not dB), freq in radian
[MAG,PHASE] = BODE(tf(b,a),w*2*pi);

amp1=[];
for(i=1:length(MAG ))
        amp1(i)=MAG (1,1,i);
end
amp1=amp1';

ph1=[];
for(i=1:length(PHASE))
        ph1(i)=PHASE(1,1,i);
end
ph1=ph1';
```

```
figure(1)                   % MATLAB invfreqs function fit
subplot(2,1,1)
hold on
plot (w,db,'b');
plot (w,20.*log10(amp1(:,1)),'r');
grid on,xlabel('Frequency [Hz]'),ylabel('Magnitude [dB]');

subplot(2,1,2)
hold on
plot (w,ph,'b');
plot (w,(ph1(:,1)),'r');
grid on, xlabel('Frequency [Hz]'),ylabel('Phase [deg]');

wM = 830*2*pi;
w1 = 938*2*pi;
w2 = 1442*2*pi;
delay = (40e-6)/2;

sysK = tf([0.0000017],[1]);                    % Scaling
sys0 = tf([1 0],[1]);                          % Vibrometer
sys1 = tf([w1^2],[1 2*0.01198*w1 w1^2]);       % 1st flexural
sys2 = tf([w2^2],[1 2*0.00798*w2 w2^2]);       % 2nd flexural
sysM = tf(-[1 2*0.0113*wM wM^2],[wM^2]);       % Correcting function
sys0.outputd = delay;
figure(2)                   % Second degree function fit
hold on
sys02 = series(sys0,sys2);
sys02 = series(sys02,sysK);
BODE(sys02,'g',w*2*pi);
hold on
sys02pade = PADE(sys02,5);
BODE(sys02pade,'k:',w*2*pi);
BODE(tf(b,a),'r',w*2*pi);

figure(3)                   % Superposition fit without the correcting function
hold on
sys012 = series(sys0,sys1);
sys012 = series(sys012,sys2);
sys012 = series(sys012,sysK);
BODE(sys012,'g',w*2*pi);
hold on
sys012pade = PADE(sys012,5);
BODE(sys012pade,'k:',w*2*pi);
BODE(tf(b,a),'r',w*2*pi);
```

```
figure(4)                    % Superposition fit with the correcting function
hold on
sys01M2 = series(sys0,sys1);
sys01M2 = series(sys01M2,sysM);
sys01M2 = series(sys01M2,sys2);
sys01M2 = series(sys01M2 ,sysK);
BODE(sys01M2,'g',w*2*pi);
hold on
sys01M2pade = PADE(sys01M2,5);
BODE(sys01M2pade,'k:',w*2*pi);
BODE(tf(b,a),'r',w*2*pi);

[MAG2,PHASE2] = BODE(sys01M2pade,w*2*pi);

amp2=[];
for(i=1:length(MAG2 ))
        amp2(i)=MAG2 (1,1,i);
end
amp2=amp2';

ph2=[];
for(i=1:length(PHASE2))
        ph2(i)=PHASE2(1,1,i);
end
ph2=ph2';

figure(5)                    % Superposition fit VS experimental data
subplot(2,1,1)
hold on
plot (w,db,'b');
plot (w,20.*log10(amp2(:,1)),'r');
grid on,xlabel('Frequency [Hz]'),ylabel('Magnitude [dB]');

subplot(2,1,2)
hold on
plot (w,ph,'b');
plot (w,ph2(:,1),'r');
grid on,xlabel('Frequency [Hz]'),ylabel('Phase [deg]');
```

APPENDIX D – "SimulinkRunner.m"

```
for k=1:7
   for l=1:7
      H=-(k-3)*2
      G=-0.03+(l-1)*0.01

      for i=1:100
         freq(i)=1440-H*40-100+2*i;

         w=freq(i);
         sim('GM_TF_LDVsys2_PosVel.mdl');    %calling the simulink model
         lng=length(velocity);
         for j=(lng-500):1:lng                % to discard the transient region
            VEL(j+501-lng)=velocity(j);
            POS(j+501-lng)=position(j);
         end
         velmax1(i)=max(VEL);
         posmax1(i)=max(POS);

      end

            figure();
      plot(freq,velmax1,'r');
      axis([1250,1700,0,4]);

            figure();
            plot(freq,posmax1,'r');
      axis([1250,1700,0,0.004]);

      velmax=max(velmax1)
      max(velmax1)/sqrt(2)
      posmax=max(posmax1)
      max(posmax1)/sqrt(2)

   end
end
```

BIBLIOGRAPHY

[1] A.Q.Liu, X.M. Zhang, V.M. Murukeshan, Q.X. Zhang, Q.B. Zou, S. Uppili, "An optical crossconnect (OXC) using drawbridge micromirrors", *Sensors and Actuators A,* vol. 97-98, pp. 227-238, 2002.

[2] A.D. Yalcinkaya , O. Ergenemanb, H. Urey, "Polymer magnetic scanners for bar code applications", *Sensors and Actuators A*, vol.135, pp. 236–243, 2007.

[3] C. Changho, I. Keiji, T. Hiroshi, "Optically modulated MEMS scanning endoscope", *IEEE photonics technology letters*, vol. 18, no: 1-4, pp. 133-135, 2006.

[4] H. Urey, "Retinal Scanning Displays", in *Encyclopedia of Optical Engineering*, R. Driggers, Editor, Marcel-Dekker, pp. 2445-2457, 2003.

[5] L. Houlet, P. Helin, T. Bourouina, G. Reyne, E.D. Gergam, H. Fujita, "Movable vertical mirror arrays for optical microswitch matrixes and their electromagnetic actuation", Presented in *Solid-State Sensor, Actuator and Microsystems Workshop* Hilton Head Island, South Carolina, June 2-6, 2002.

[6] Y. Okano, Y. Hirabayashi, "Magnetically actuated micromirror and measurement system for motion characteristics using specular reflection" *IEEE Journal on Selected Topics in Quantum Electronics,* vol. 8, no.1, January/February 2002.

[7] H.Y. Lin, W. Fang, "A Rib-reinforced micro torsional mirror driven by electrostatic torque generators", *Sensors and Actuators A*, vol. 105, pp.1-9, 2003.

[8] D.Lee, U. Krishnamoorty, K.Yu, O. Solgaard, "Single crystalline silicon micromirrors actuated by self aligned vertical electrostatic combdrives with piston motion and rotation capability", *Sensors and Actuators A,* vol. 114, pp. 423-428, 2004.

[9] S. Schweizer, S. Calmes, M. Laudon, Ph. Renaud, "Thermally actuated optical microscanner with large angle and low consumption", *Sensors and Actuators*, vol. 76, pp. 470-477, 1999.

[10] K.H. Chau, S. Dimitrijev, "Two-dimensional microscanner actuated by PZT thin film," *SPIE Proc. of Device and Process Technologies for MEMS and Microelectronics*, vol. 3892, pp. 133-140, October 1999.

[11] S.Holmstrom, A.D. Yalcinkaya, S. Isikman, C. Ataman, H. Urey, "FR4 as a New MOEMS Platform", *IEEE/LEOS International Conference on Optical MEMS and Nanophotonics*, pp. 25-26, 2007.

[12] S. Pannu, C. Chang, R.S. Muller, and A.P. Pisano, "Closed-Loop Feedback Control System for Improved Tracking in Magnetically Actuated Micromirrors", *IEEE/LEOS International Conference on Optical MEMS*, pp. 107-108, 2000.

[13] I. Gunev, A. Varol, S. Karaman, C. Basdogan, "Adaptive Q control for tapping-mode nanoscanning using a piezoactuated bimorph probe*", Review of scientific instruments*, vol. 78, no:4, 043707.1-8, 2007.

[14] S. Park, R. Horowitz, "Adaptive control for z-axis MEMS gyroscopes", *American Control Conference*, Arlington, VA, USA, pp. 496–501, June 25-27, 2001.

[15] T. Kobayashi, R. Maeda, T. Itoh, R. Sawada, "Smart optical microscanner with piezoelectric resonator, sensor, and tuner using Pb(Zr,Ti)O3 thin film", *Applied Physics Letters* 90, 183514, 2007.

[16] C.T.C. Nguyen, R.T. Howe, "Quality factor control for micromechanical resonators", *In Tech. Dig. IEEE Int. Electron Devices Meeting*, San Francisco, CA, pp. 505–508, December 14–16, 1992.

[17] H.M. Cheng, M.T.S. Ewe, G.T.C. Chiu, R. Bashir, "Modeling and control of piezoelectric cantilever beam micro-mirror and micro-laser arrays to reduce image banding in electrophotographic processes", *Journal of Micromechanics Microengineering*, vol.11, pp. 487–498, 2001.

[18] D. H. S. Maithripala, J. M. Berg, W. P. Dayawansa, "Control of an Electrostatic Microelectromechanical System Using Static and Dynamic Output Feedback", *ASME Journal of Dynamical Systems, Measurement and Control*, vol. 127, no: 3, pp. 443-450, 2005.

[19] I. Veryeri, I. Basdogan , "Dynamic Characterization and Damping Control of a MEMS Structure", *SPIE, International Syposium on Optomechatronic Technologies*, Lausanne, Switzerland, October 2007.

[20] O. Anac, I. Basdogan, "Model Validation and Performance Prediction in the Design of Micro Systems," *Journal of Vibration and Control*, vol.14, no:11, pp.1711-1728, 2008.

[21] E.M.Lawrence, K. Speller, D. Yu, "Laser Doppler vibrometry for optical MEMS", *Fifth International Conference on Vibration Measurements by Laser Techniques: Advances and Applications*, Proc. SPIE, vol. 4827, pp. 80-87, 2002.

[22] Y. Zhao, F.E.H. Tay, G. Zhou, F.S. Chau, "Fast and precise positioning of electrostatically actuated dual-axis micromirror by multi-loop digital control", *Sensors and Actuators A*, vol.132, pp. 421-428, 2006.

[23] Polytec OFV-551/552 Fiber Optic Interferometer Datasheet

[24] http://www.cadence.com/products/orcad/pspice_simulation/pages/default.aspx

[25] Polytec Manual Microscope Scan Unit, MSV-50, User Manual

[26] http://www.ni.com/labview/

[27] http://www.mathworks.com/

[28] ME'scope VES Operating Manual, Version 3.0, September 2001

[29] S.S. Rao, *Mechanical Vibrations*, Pearson Education, 2004.

PUBLICATIONS

I. Veryeri, I. Basdogan, “Dynamic Characterization and Damping control of a MEMS Structure”, *Proceedings of ISOT 2007, International Symposium on Optomechatronic Technologies*, October, 2007, Lausanne, Switzerland.

I. Veryeri, I. Basdogan, “Adjusting the Vibratory Response of a Micro Mirror via Position and Velocity Feedback”, submitted to *Journal of Vibration and Control*, October, 2008.

VITA

Ilgar Veryeri was born in İstanbul, Turkey, in 1982. He received his B.Sc. degree from Mechanical Engineering Department of Middle East Technical University, Ankara, in 2006. Same year, he joined the Department of Mechanical Engineering at Middle East Technical University as an M.Sc. candidate. In the spring semester of 2007, he joined the Department of Mechanical Engineering at Koç University, İstanbul as a transfer student.